The Astrophysical Journal, 972:162 (21pp), 2024 September 10 https://doi.org/10.3847/1538-4357/ad5e7b

Gamma-Ray Bursts Observed by the Transiting Exoplanet Survey Satellite: Prompt Optical Counterparts and Afterglows of Swift-XRT-localized Gamma-Ray Bursts

Rahul Jayaraman[1], Michael Fausnaugh[1,2], George R. Ricker[1], Roland Vanderspek[1], and Geoffrey Mo[1,3]

[1] Department of Physics and Kavli Institute for Astrophysics and Space Research, Massachusetts Institute of Technology, 77 Massachusetts Ave., Cambridge, MA 02139, USA; rjayaram@mit.edu

[2] Department of Physics and Astronomy, Box 41051, Texas Tech University, Lubbock, TX 79409, USA

[3] LIGO Laboratory, Massachusetts Institute of Technology, 185 Albany St., Cambridge, MA 02139, USA

Received 2023 December 11; revised 2024 June 24; accepted 2024 June 25; published 2024 September 4

Abstract

Very few detections have been made of optical flashes contemporaneous with prompt high-energy emission from a gamma-ray burst (GRB). In this work, we present and analyze light curves of GRB-associated optical flashes and afterglows from the Transiting Exoplanet Survey Satellite (TESS). Our sample consists of eight GRBs with arcsecond-level localizations from the X-Ray Telescope on board the Neil Gehrels Swift Observatory (Swift). For each burst, we characterize the prompt optical emission and any observed afterglow, and constrain physical parameters for four of these bursts using their TESS light curves. This work also presents a straightforward method to correct for TESS's cosmic-ray mitigation strategy on 20 s timescales, which allows us to estimate the "true" brightness of optical flashes associated with prompt GRB emission. We also highlight TESS's continuous wide-field monitoring capability, which provides an efficient means of identifying optical emission from GRBs and characterizing early time afterglow light curves. Based on empirical detection rates from Swift and the Fermi Gamma-ray Space Telescope, up to 10 GRBs per year may fall within the contemporaneous TESS field of view.

Unified Astronomy Thesaurus concepts: Gamma-ray bursts (629); Transient sources (1851)

Materials only available in the online version of record: machine-readable table

1. Introduction

Gamma-ray bursts (GRBs) are the most energetic explosions in the Universe, releasing over 10^{51} erg of energy solely in gamma rays (Frail et al. 2001). These intense transients, typically occurring at cosmological distances, exhibit a bimodal distribution in their duration (Kouveliotou et al. 1993) that is connected to the nature of the progenitor. Short GRBs ($\lesssim$2 s) are typically caused by neutron star mergers (see, e.g., Eichler et al. 1989; Berger 2014), while long GRBs ($\gtrsim$10 s) canonically result from the core-collapse supernovae of low-metallicity stars with stripped hydrogen envelopes (Woosley & Bloom 2006; Cano et al. 2017), but some could arise from neutron star mergers (Rastinejad et al. 2022; Levan et al. 2024a). Long GRBs can often exhibit multiple emission episodes (e.g., Gendre et al. 2013).

Thousands of GRBs have been detected in the decades since the first observations by the Vela satellites (Klebesadel et al. 1973). These detections have been enabled by numerous high-energy sky-monitoring satellites, including the Burst and Transient Source Experiment on board the Compton Gamma-Ray Observatory (e.g., Preece et al. 2000), the BeppoSAX mission (Feroci et al. 1997), the High-Energy Transient Explorer-2 (Ricker et al. 2003), the Neil Gehrels Swift Observatory (Swift; Gehrels et al. 2004), and the Fermi Gamma-ray Space Telescope (Atwood et al. 2009; Meegan et al. 2009).

GRBs have been confidently associated with rapidly decaying optical transients ("afterglows") following the discovery of one associated with GRB 970228 (van Paradijs et al. 1997; Wijers et al. 1997). Afterglows arise from the cooling and expanding ejecta shocking the circumburst medium (Mészáros & Rees 1997; Sari et al. 1998). Since GRB 970228, ~1000 optical afterglows have been detected.[4] Since the 1990s, the identification of prompt optical counterparts and afterglows has been enabled by the rapid distribution of GRB localizations via the General Coordinates Network (GCN).[5]

While the detection of numerous optical afterglows has shed light on the diversity of GRBs and the evolution of their ejecta at late times, it has been more difficult to identify optical counterparts contemporaneous with the high-energy emission from the GRB. Such episodes are often referred to as "prompt" optical emission. Searches for prompt emission began in the 1990s, with early upper limits on the prompt optical flux established by the Gamma-Ray Optical Counterpart Search Experiment and its successor, the Livermore Optical Transient Imaging System (LOTIS; Park et al. 1997a, 1997b). The first detection of prompt emission, in GRB 990123, was made using the Robotic Optical Transient Search Experiment (Akerlof et al. 1999). The next detection occurred 5 yr later: prompt optical emission from GRB 041219A (Blake et al. 2005; Vestrand et al. 2005) was detected by both the RAPid Telescopes for Optical Response (RAPTOR) network (Vestrand et al. 2002) and the Peters Automated Infrared Imaging Telescope (Bloom et al. 2006). RAPTOR also detected prompt emission from GRB 050820A (Vestrand et al. 2006).

In the 2000s, several more optical counterparts were found by LOTIS (Williams et al. 2008). Concurrently, the Télescopes

---

[4] An unofficial catalog of well-localized GRBs can be found at https://www.mpe.mpg.de/~jcg/grbgen.html, along with information about afterglow detections in X-ray, optical, and radio.

[5] https://gcn.nasa.gov/circulars

à Action Rapide pour les Objets Transitoires network (Klotz et al. 2009) placed upper limits on prompt optical flux from other GRBs and detected prompt emission from GRB 060111B (Klotz et al. 2006). Early time optical observations of GRB 080319B (Racusin et al. 2008) by Pi of the Sky (Burd et al. 2005) and Telescopio Ottimizzato per la Ricerca dei Transienti Ottici RApidi (Molinari et al. 2006) showed a clear distinction between prompt emission, reverse shock, and afterglow in the light curve. Since GRB 080319B, only a few prompt optical counterparts have been detected (Vestrand et al. 2014; Troja et al. 2017; Zhang et al. 2018; Becerra et al. 2021; Oganesyan et al. 2023; Xin et al. 2023).

The physical mechanism underlying prompt optical emission remains poorly understood. Mészáros & Rees (1999) suggested that the prompt optical flash from GRB 990123 arose from internal shocks, or a reverse shock from the blast wave generated by the GRB interacting with the circumburst medium (also discussed in Kobayashi 2000). Modeling of the reverse shock hypothesis (Mészáros & Rees 1997; Sari & Piran 1999a) found that a reverse shock would have an energy comparable to the forward shock, but radiate at optical wavelengths. Other possibilities for the prompt optical emission include synchrotron self-Compton upscattering (Panaitescu & Kumar 2007) and inverse Compton scattering in the thermal plasma behind the forward shock (Beloborodov et al. 2014).

In an ensemble analysis of prompt optical emission from GRBs, Kopač et al. (2013) suggested that synchrotron radiation from shocks internal to the jet could explain the observed optical flashes. Oganesyan et al. (2019) analyzed a sample of 21 GRBs, some with both prompt optical observations and early time data from the Swift X-Ray Telescope (Swift-XRT); half of their sample had gamma-ray through optical spectra consistent with synchrotron emission.

The paucity of prompt optical detections of GRBs reflects the difficulty of detecting such emission serendipitously from the ground. Telescopes must be observing the particular region of sky in which a GRB occurs at the time of trigger (e.g., Xin et al. 2023), or rapidly slew to tile the initial localization of the GRB (e.g., Akerlof et al. 1999; Vestrand et al. 2005). These issues can be mitigated by space-based optical observatories with large fields of view (FOVs), which can continuously monitor emissions from the minutes to hours before the explosion, through the time of the GRB trigger, and after cessation of the prompt gamma-ray emission. Such continuous observations allow for the identification of prompt optical counterparts, the afterglow, and late-time emission such as kilonovae (Abbott et al. 2017) or supernovae (Galama et al. 1998). These observations could also constrain the existence of optical precursors, which have never been observed (Blake & Bloom 2004; Piotrowski 2012), but may relate to the gamma-ray precursors that are seen in ∼20% of bursts (Koshut et al. 1995; Lazzati 2005; Burlon et al. 2008; Coppin et al. 2020).

In this work, we searched for optical emission from 22 GRBs with arcsecond-level localizations from Swift-XRT in data from the Transiting Exoplanet Survey Satellite (TESS). Of these, we detected nine bursts with optical emission. Section 2 discusses the TESS observations, high-energy data, and our searches for optical emission. Section 3 presents our power-law fits to the afterglows and constraints on the brightness of optical flashes at the time of the GRB trigger. Section 4 interprets the light curves and constrains burst parameters. Finally, Section 5 discusses the utility of TESS for GRB science.

2. TESS Observations of Gamma-Ray Bursts

TESS is an all-sky survey whose primary aim is to detect transiting exoplanets orbiting bright stars (Ricker et al. 2015). Launched in 2018 April, TESS observes a given 2304 deg^2 region of the sky for ∼28 days at a time (a period known as a "sector").[6] During the first 5 yr of the mission, TESS observed over 90% of the sky, and revisited fields roughly every other year. TESS's CCD detectors have a plate scale of $21''$ pixel^{-1}.

During its Prime Mission, from 2018 July to 2020 July (Sectors 1–26), TESS obtained images of its entire FOV; these are referred to as full-frame images (FFIs). FFIs were recorded at a cadence of 1800 s. During TESS's Extended Mission 1, from 2020 July to 2022 September (Sectors 27–55), the FFI exposure times were shortened to 600 s. Starting in 2022 September, TESS's Extended Mission 2 (Sectors 56–83) further reduced the FFI cadence to 200 s and added weekly data downlinks—making TESS much more useful for timely follow-up of fast transients such as GRBs.

TESS's ability to continuously monitor over 2000 deg^2 of the sky for at least a month at a time is useful for detecting prompt optical flashes from GRBs and other associated emission. TESS data have already been used to study individual GRBs and their afterglows: Smith et al. (2021) analyzed the afterglow of GRB 191016A; Fausnaugh et al. (2023a) presented a TESS light curve of GRB 230307A, with a prompt flash preceding a fainter afterglow; and Roxburgh et al. (2023) identified four GRB afterglows in TESS data.

2.1. Sample Selection

We analyzed GRBs from the Swift-XRT catalog (Evans et al. 2009)[7]—which includes GRBs localized to within $\lesssim 10''$ (Goad et al. 2007)—and identified 22 GRBs where the trigger time and localization coincided with TESS observations of that sky region. Our search spanned the first 5 yr of the TESS mission—from the start of Sector 1 in 2018 July, to the end of TESS Sector 69, in 2023 September. An additional 39 bursts were detected by the Swift Burst Alert Telescope (Swift-BAT) over the time period in consideration that lacked a corresponding XRT detection. None of these arcminute-level localizations fell within the contemporaneous TESS FOV. The list of TESS-coincident GRBs, including coordinates, trigger times, and GRB properties, is given in Table 1.

2.2. TESS Light Curves

We extract TESS light curves of GRBs using the FFIs generated by the TESS Image CAlibrator (TICA; Fausnaugh et al. 2020). We first build a reference image from the median of 20 FFIs that have a low background, and then subtract the reference from the other FFIs using the ISIS image subtraction package (Alard & Lupton 1998). Then, for each GRB, we perform forced photometry on the generated difference images at the GRB coordinates. Both the difference imaging and photometry procedures are detailed in Fausnaugh et al. (2021, 2023b). The observed counts are then converted to TESS Vega magnitudes (T), and then to janskys (F_ν). To do so, we calculated the Vega zero-point in the TESS bandpass using the CALSPEC Vega model (Bohlin 2014), as implemented in

---

[6] Information about TESS pointings is available at https://tess.mit.edu/observations/.

[7] https://www.swift.ac.uk/xrt_live_cat/

Table 1

GRBs with Swift-XRT Localizations Falling within the TESS Field of View at the Time of Trigger

Identifier	Coordinates (J2000)						Trigger		GRB Properties		3σ Limit ($T_{\rm mag}$)	E_{B-V} (mag)	Extinction Correction
	R.A.			Decl.			BTJD	Sector	T_{90} (s)	σT_{90}			
GRB 180727A	$23^{\rm h}$	$06^{\rm m}$	$39^{\rm s}.84$	$-63^{\rm d}$	$03^{\rm m}$	$06^{\rm s}.48$	1327.09850	1	1.1 (a)	0.2	18.74	0.019	0.965
GRB 180924A	$03^{\rm h}$	$16^{\rm m}$	$47^{\rm s}.87$	$-58^{\rm d}$	$31^{\rm m}$	$57^{\rm s}.00$	1386.14331	3	95.1 (b)	10.9	19.01	0.025	0.955
GRB 181022A	$03^{\rm h}$	$47^{\rm m}$	$09^{\rm s}.94$	$-29^{\rm d}$	$22^{\rm m}$	$56^{\rm s}.28$	1414.23386	4	6.74 (c)	2.30	18.98	0.012	0.979
GRB 190422A	$12^{\rm h}$	$08^{\rm m}$	$08^{\rm s}.42$	$-60^{\rm d}$	$13^{\rm m}$	$27^{\rm s}.48$	1596.45954	10	213.25 (d)	10.75	17.98	1.402	0.089
GRB 190630C	$19^{\rm h}$	$35^{\rm m}$	$31^{\rm s}.25$	$-32^{\rm d}$	$44^{\rm m}$	$38^{\rm s}.04$	1665.50153	13	38.4 (e)	9.3	17.88	0.099	0.833
GRB 191016A (f)	$02^{\rm h}$	$01^{\rm m}$	$04^{\rm s}.65$	$+24^{\rm d}$	$30^{\rm m}$	$35^{\rm s}.68$	1772.67919	17	219.70 (g)	183.35	18.76	0.094	0.841
GRB 200303A	$14^{\rm h}$	$10^{\rm m}$	$52^{\rm s}.54$	$+51^{\rm d}$	$21^{\rm m}$	$33^{\rm s}.37$	1911.61090	22	94.2 (h)	6.4	19.08	0.014	0.975
GRB 200324A	$14^{\rm h}$	$50^{\rm m}$	$41^{\rm s}.71$	$+35^{\rm d}$	$56^{\rm m}$	$29^{\rm s}.98$	1933.19817	23	⋯ (i)	⋯	18.87	0.012	0.977
GRB 200412B	$18^{\rm h}$	$33^{\rm m}$	$15^{\rm s}.19$	$+62^{\rm d}$	$31^{\rm m}$	$57^{\rm s}.00$	1951.88161	23	6.08 (d)	0.29	18.88	0.050	0.911
GRB 200901A	$04^{\rm h}$	$07^{\rm m}$	$07^{\rm s}.96$	$-59^{\rm d}$	$53^{\rm m}$	$26^{\rm s}.88$	2093.65995	29	20.37 (j)	7.55	18.67	0.014	0.975
GRB 210204A (k)	$07^{\rm h}$	$48^{\rm m}$	$19^{\rm s}.34$	$+11^{\rm d}$	$24^{\rm m}$	$33^{\rm s}.98$	2249.77660	34	206.85 (d)	2.29	18.19	0.028	0.949
GRB 210222B	$10^{\rm h}$	$18^{\rm m}$	$25^{\rm s}.37$	$-14^{\rm d}$	$55^{\rm m}$	$54^{\rm s}.12$	2268.44869	35	12.82 (l)	1.28	⋯	0.089	0.848
GRB 210419A	$05^{\rm h}$	$47^{\rm m}$	$24^{\rm s}.18$	$-65^{\rm d}$	$30^{\rm m}$	$07^{\rm s}.92$	2323.78791	37	64.43 (m)	11.69	$\sim$17.5	0.066	0.884
GRB 210504A	$14^{\rm h}$	$49^{\rm m}$	$33^{\rm s}.84$	$-30^{\rm d}$	$32^{\rm m}$	$00^{\rm s}.24$	2339.08622	38	135.06 (n)	9.57	18.24	0.122	0.798
GRB 210730A	$09^{\rm h}$	$58^{\rm m}$	$22^{\rm s}.08$	$+69^{\rm d}$	$41^{\rm m}$	$22^{\rm s}.09$	2425.70386	41	3.86 (o)	0.66	17.66	0.074	0.872
GRB 220319A	$14^{\rm h}$	$32^{\rm m}$	$53^{\rm s}.86$	$+61^{\rm d}$	$17^{\rm m}$	$43^{\rm s}.30$	2658.23949	49	6.44 (p)	1.54	18.19	0.009	0.983
GRB 220623A	$09^{\rm h}$	$41^{\rm m}$	$34^{\rm s}.49$	$+75^{\rm d}$	$49^{\rm m}$	$15^{\rm s}.60$	2753.79238	53	57.11 (q)	8.53	18.16	0.032	0.942
GRB 220708A	$06^{\rm h}$	$52^{\rm m}$	$30^{\rm s}.17$	$+72^{\rm d}$	$08^{\rm m}$	$28^{\rm s}.00$	2768.69110	53	4.4 (r)	1.0	17.99	0.152	0.755
GRB 221120A	$02^{\rm h}$	$45^{\rm m}$	$21^{\rm s}.56$	$+43^{\rm d}$	$14^{\rm m}$	$35^{\rm s}.27$	2904.40134	58	0.79 (s)	0.16	17.61	0.082	0.860
GRB 230116D	$06^{\rm h}$	$34^{\rm m}$	$28^{\rm s}.28$	$+49^{\rm d}$	$52^{\rm m}$	$22^{\rm s}.30$	2961.38386	60	41.00 (t)	11.18	17.84	0.100	0.832
GRB 230307A (u)	$04^{\rm h}$	$03^{\rm m}$	$26^{\rm s}.24$	$-75^{\rm d}$	$22^{\rm m}$	$43^{\rm s}.68$	3011.15549	62	34.56 (d)	0.57	17.87	0.077	0.867
GRB 230903A	$00^{\rm h}$	$39^{\rm m}$	$38^{\rm s}.81$	$-40^{\rm d}$	$56^{\rm m}$	$57^{\rm s}.48$	3191.22939	69	2.54 (v)	0.27	17.83	0.011	0.980

Notes. These GRBs occurred between the start of the TESS mission (in 2018 July) and 2023 September, corresponding to all of TESS Sectors 1–69. The nine GRBs with detections in TESS are highlighted in bold. The barycentric TESS Julian date (BTJD) is defined as JD – TDB – 2457000, and is measured at the solar system barycenter. JD – TDB is the barycentric dynamical time (TDB) standard as detailed in Eastman et al. (2010). GRB coordinates are obtained from the Swift-XRT GRB Catalog (https://www.swift.ac.uk/xrt_live_cat/), which contains analyses based on Evans et al. (2009). For all GRBs, we note the 3σ detection threshold, calculated based on the rms scatter in the light curve before the trigger. Entries with "..." indicate that there was no information available for the T_{90} parameter, or that the GRB occurred during an observing gap in TESS, precluding a calculation of the limiting magnitude. E_{B-V} extinction values, calculated using the reddening maps from Schlafly & Finkbeiner (2011) and the coefficients from Cardelli et al. (1989), account only for Galactic extinction. The measured flux was divided by the extinction correction factor (enumerated in the last column) to estimate the unattenuated flux values; details of this calculation are provided in Section 2.2. Horizontal lines indicate changes in the TESS FFI cadence, from 1800 s to 600 s, and from 600 s to 200 s.

References. (a) Lien et al. (2018). (b) Stamatikos et al. (2018a). (c) Stamatikos et al. (2018b). (d) Fermi Gamma-ray Burst Monitor (GBM) Burst Catalog (FERMIGBRST) Gruber et al. (2014); Narayana Bhat et al. (2016). (e) Krimm et al. (2019); von Kienlin et al. (2014, 2020). (f) Analyzed and discussed in Smith et al. (2021). (g) Barthelmy et al. (2019). (h) Palmer et al. (2020). (i) Ukwatta et al. (2020). (j) Sakamoto et al. (2020). (k) This GRB was associated with the ZTF-triggered optical transient AT2021buv/ ZTFaagwbjr, discovered with ZTFReST (Andreoni et al. 2021). The ZTF light curve was analyzed in Kumar et al. (2022) and Ho et al. (2022). (l) Ukwatta et al. (2021). (m) Palmer et al. (2021). (n) Laha et al. (2021). (o) Sakamoto et al. (2021). (p) Krimm et al. (2022). (q) Parsotan et al. (2022). (r) Barthelmy et al. (2022). (s) Sakamoto et al. (2022). (t) Markwardt et al. (2023). (u) Fausnaugh et al. (2023a), Yang et al. (2024). (v) Moss et al. (2023), Levan et al. (2024a).

the synthetic photometry package `synphot` (STScI Development Team 2018). We found that a TESS Vega magnitude of $T = 0$ corresponds to a flux of 2583 Jy. Thus, the equations to calculate T[8] and F_ν are

$$T = -2.5\log_{10}\left(\frac{N}{t \times 0.99 \times 0.8}\right) + 20.44, \quad \text{and} \tag{1}$$

$$F_\nu = 2583\ \text{Jy} \times 10^{-T/2.5}, \tag{2}$$

respectively. Here, N is the total observed counts from a source in a given FFI, and t is the observational cadence (exposure time). The factors of 0.99 and 0.8 arise from the frame transfer efficiency and the cosmic-ray mitigation (CRM) process, respectively. CRM is further discussed in Section 2.4 and the Appendix. In Table 2, we present light curves spanning from 0.5 days pretrigger to 1.5 days posttrigger for the eight GRBs from Swift-XRT with confident detections in TESS; the light curves in the table include both differential counts and F_ν (given in units of Jy). These are flux calibrated, i.e., the light curve has been shifted to ensure a baseline of 0 counts by subtracting the mean value of the out-of-burst light curve (assuming a constant background term).

We then corrected for Galactic extinction as follows: First, we assumed an intrinsic power-law spectrum for the GRB of the form $F_0(\nu) \propto \nu^{-1}$, and calculated the response in the TESS bandpass[9] using `synphot`. We then calculated the extinction of the input spectrum in the TESS bandpass using a Cardelli et al. (1989) extinction law (with $R_V = 3.1$, which is handled by the `mwavg` option in `synphot`), and E_{B-V} values from Schlafly & Finkbeiner (2011).[10] The relationship between the

---

[8] The TESS "zero-point" of 20.44, corresponding to a detector count rate of 1 $e^- s^{-1}$, has an uncertainty of 0.05 that propagates to all our magnitude estimates (Fausnaugh et al. 2021). This was calculated from the equivalence in the TESS instrument handbook (linked in footnote 10) where 15,000 $e^- s^{-1}$ corresponds to $T = 10$.

[9] https://heasarc.gsfc.nasa.gov/docs/tess/data/tess-response-function-v2.0.csv

[10] These are from the online extinction calculator hosted by the NASA/IPAC Extragalactic Database (https://ned.ipac.caltech.edu/extinction_calculator).

Table 2
TESS Light Curves of the Eight Gamma-Ray Bursts Analyzed in This Work

GRB Identifier	BTJD (BJD – 2457000)	Diff. Flux	Uncertainty	T_{mag}	Uncertainty	Flux	Uncertainty	Background (counts s^{-1})
		(counts s^{-1})				(mJy)		
200412B	1951.38554	−0.777	0.564	18.880	⋯	⋯	⋯	1.298
200412B	1951.40637	0.939	0.559	18.880	⋯	⋯	⋯	0.656
200412B	1951.42721	−1.098	0.555	18.880	⋯	⋯	⋯	0.146
200412B	1951.44804	−1.418	0.554	18.880	⋯	⋯	⋯	0.065
200412B	1951.46888	−1.194	0.564	18.880	⋯	⋯	⋯	0.713
200412B	1951.48971	−0.715	0.551	18.880	⋯	⋯	⋯	0.445
200412B	1951.51054	1.663	0.549	18.787	0.340	0.079	0.029	2.166

Notes. The light curves start 0.5 days before the trigger, and end 1.5 days posttrigger. We report the flux in counts, magnitudes, and provide the F_ν (in units of Jy), along with these values' associated uncertainties. We also include the background estimate from our photometry routine. For cadences with nondetections, we include the limiting T_{mag} and a "..." in the flux and uncertainty columns. Flux values for nondetections are left blank in the machine-readable table

(This table is available in its entirety in machine-readable form in the online article.)

extinction in the TESS bandpass and the V band (from Landolt 1992) is given by

$$A_{\mathrm{TESS}} = (-0.0097 \pm 0.0475)A_V{}^2 + (0.6470 \pm 0.3047)A_V + (0.0025 \pm 0.4087). \qquad (3)$$

We also calculated the conversion from TESS Vega magnitudes to AB magnitudes

$$T_{\mathrm{AB}} = (0.3697 \pm 0.0001) + T_{\mathrm{Vega}}. \qquad (4)$$

Finally, we recalculated the response in the TESS bandpass of the extinguished spectrum; the ratio of the unextinguished to extinguished flux yields the correction factor for the observed GRB light curves, given in the rightmost column of Table 1. The column to its left gives the E_{B-V} values used in this calculation.

After correcting for extinction, we then calculated the monochromatic flux νF_ν, where ν is the frequency corresponding to the pivot wavelength of the TESS bandpass (784 nm), calculated using `synphot`. All flux values reported throughout this work are in νF_ν (with physical units of erg $\mathrm{cm}^{-2}\ \mathrm{s}^{-1}$), where ν is the corresponding central frequency of the TESS bandpass, 3.824×10^{14} Hz. We define BTJD as JD – TDB – 2457000, where JD – TDB is a time system in which times are measured at the solar system barycenter (Eastman et al. 2010). Further information on timing corrections is given in Section 2.4.2.

2.3. Identifying Gamma-Ray Burst Signals in TESS

After flux-calibrating the TESS light curves for our sample of 22 GRBs, we looked for signatures of prompt and afterglow emission by both visual inspection and searching for any cadences exhibiting a $>3\sigma$ flux excess within ±0.2 days of the GRB trigger; this excess was calculated relative to the rms scatter of the light-curve baseline before the trigger, using a window of 0.5 days in a flat portion of the light curve. We identified such an excess for nine GRBs; we chose to exclude GRB 191016A from our sample, as it had been analyzed in Smith et al. (2021). Figures 1 and 2 show light curves in both counts and magnitude for the other eight GRBs.

Some notes about the data for specific GRBs follow.

1. GRB 200901A could be contaminated by the flux from a $T = 15.6$ source within 30″ (1.5 TESS pixels) of the GRB position (TIC 358253511).
2. GRB 210222B occurred in the observing gap during data downlink in Sector 35; hence, there are no data at the time of burst. However, we still searched for afterglow emission from this GRB in TESS, given the confident afterglow detections reported via GCN (e.g., Hu et al. 2021; Strausbaugh & Cucchiara 2021). This GRB also occurred less than 3 TESS pixels (1′) away from the known variable star TIC 385212568, with a magnitude of $T = 11.4$.
3. GRB 210419A suffers significant contamination from a nearby variable star (TIC 149597885; 7″ sky separation, or $\lesssim$0.5 TESS pixels) with magnitude $T = 15.9$. The variability in this star is clearly visible in light curves from previous sectors.
4. Data for GRB 220623A were affected by time-varying backgrounds from earthshine around and after the time of trigger.
5. GRB 230116D is less than 3 TESS pixels (60″) away from a $T = 13.5$ magnitude star, TIC 253030410. Other nearby faint stars (which have $T \sim 18$) may also add noise to the light curve.

We also note that the 1800 s cadence during TESS's Prime Mission and, to some extent, the 600 s cadence during the Extended Mission 1, may obscure the different phases of GRB emission. For instance, an 1800 s FFI spanning the time of trigger may contain contributions from the prompt emission and the early afterglow. For GRBs where this is the case, we attempted to remove the afterglow's contribution to the fluence; more details are given in the text describing the analysis for each GRB.

2.4. Analysis of Prompt Emission

The TESS FFI exposure times throughout the mission of 1800 s, 600 s, and 200 s, are are typically much longer than the prompt gamma-ray emission from a burst (see, e.g., Figure 1 from Tarnopolski 2015). Consequently, if the prompt optical emission were to have the same temporal profile as the high-energy emission (as was observed in Vestrand et al. 2005, 2014; Racusin et al. 2008, for photons between 15 and 350 keV), the flux measured by TESS would underestimate the actual flux, due to the exposure time being

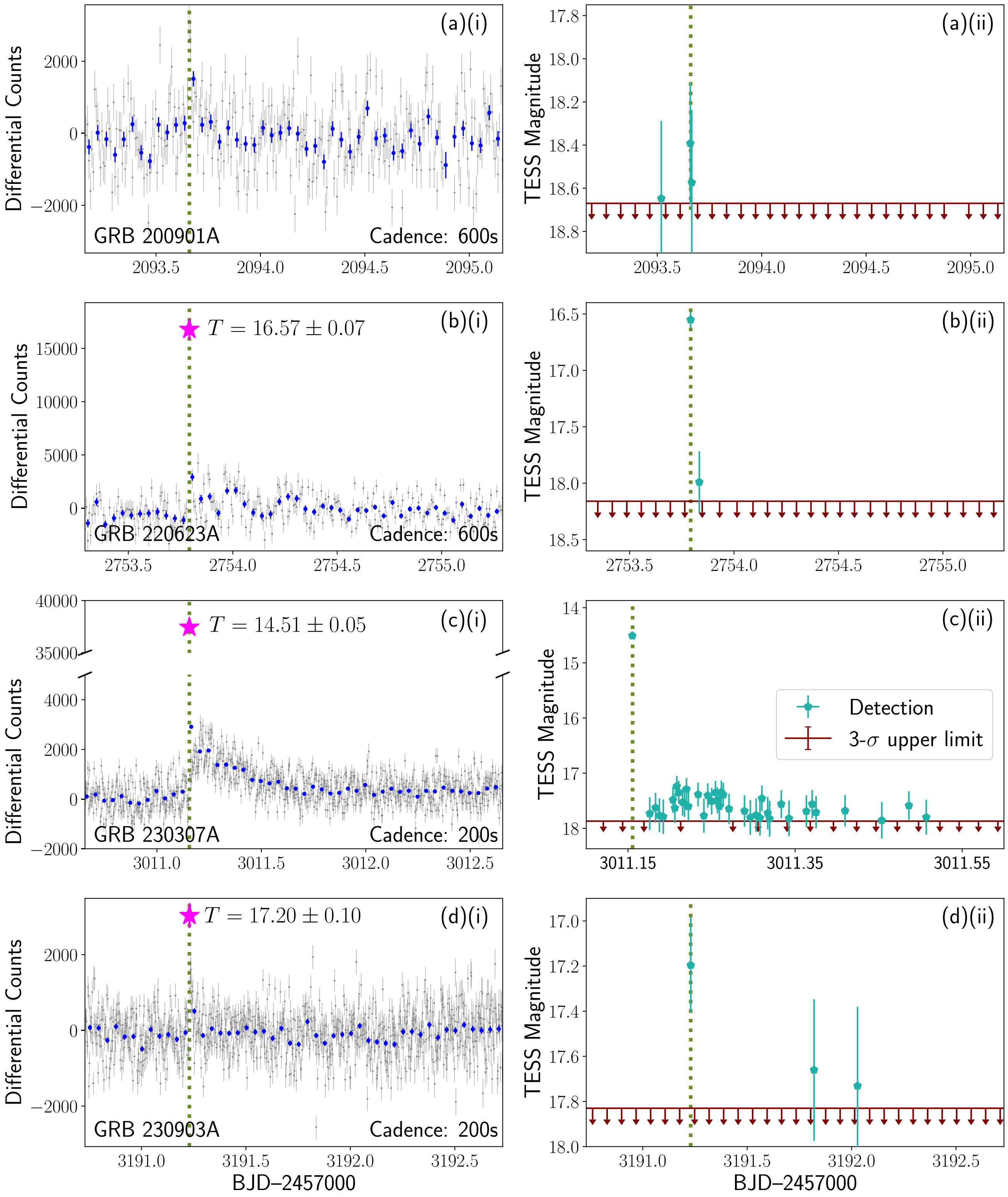

Figure 1. TESS light curves of Swift-XRT-localized GRBs with prompt emission detected at the 3σ level in the TESS difference images (see Section 2.3 for further information). The left panel shows the flux in raw counts, as measured in the difference images; zero is the flux in the reference image (constructed using the procedure described in Fausnaugh et al. 2021, 2023b). The flux at the native cadence is shown in light gray, while the light curve binned to 1 hr is shown in blue. The right panel shows the light curve in magnitudes—the pentagons correspond to 3σ detections of a source, while the arrows represent upper limits on the flux. Magnitudes were calculated by shifting the observed light curve (in counts) so that the out-of-burst portion was at zero flux; uncertainties were rescaled to be consistent with the rms scatter. The time of each trigger is indicated by the green dotted line, and likely detections of prompt emission are indicated by a pink star in the left panels.

considerably longer than the duration of the burst itself. The magnitude of this effect can be estimated to zeroth order from the ratio of the GRB duration to the FFI exposure time. The GRB's duration is estimated typically with the T_{90} parameter, the time interval during which 90% of its prompt high-energy flux is emitted.

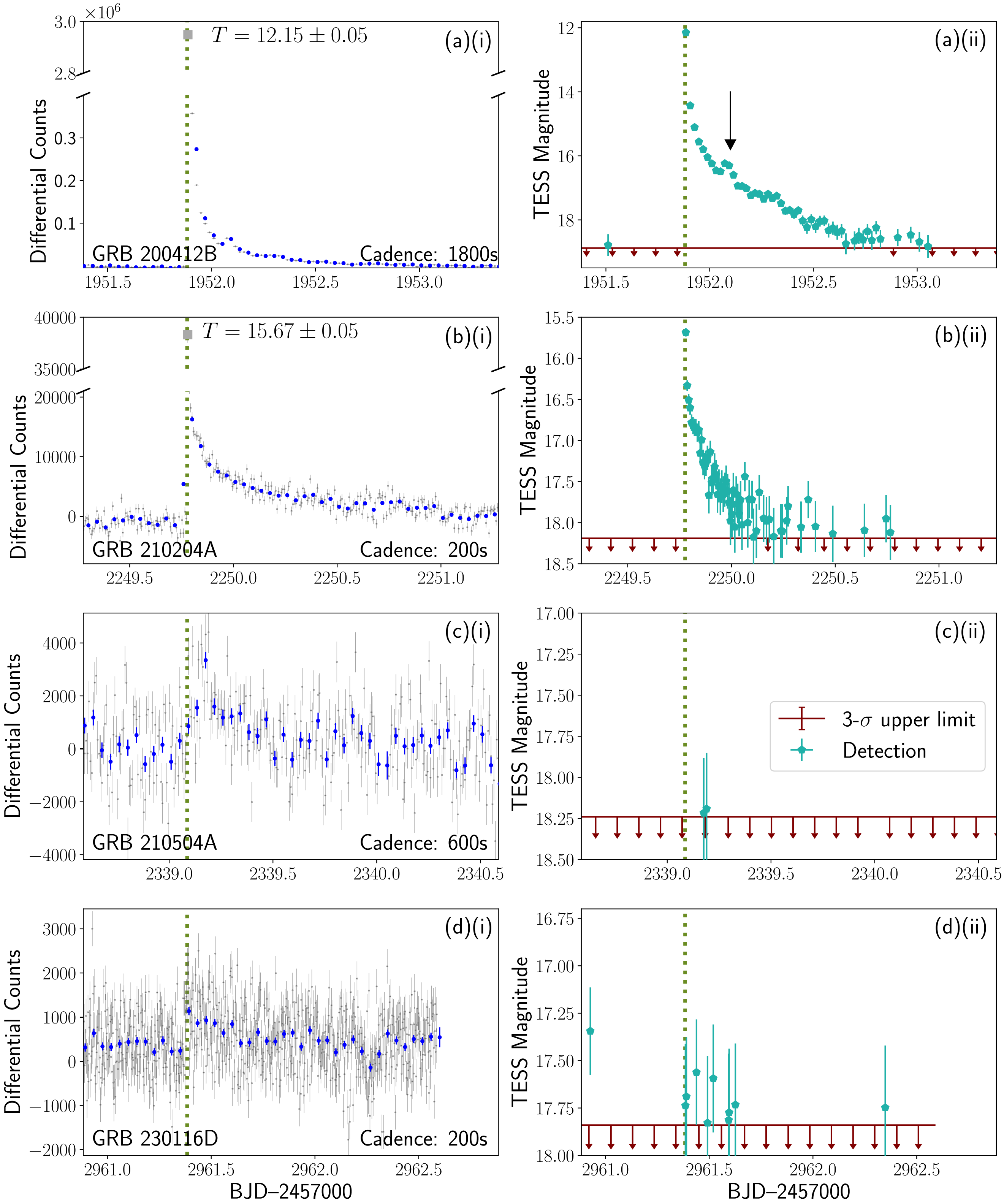

Figure 2. As Figure 1, but for bursts without a clear detection of prompt emission in a single cadence. This figure also includes lower-significance detections of possible afterglows, such as GRBs 210504A and 230116D in panels (c) and (d), respectively. The gray squares in panels (a)(i) and (b)(i) represent detections that likely have some contribution from prompt emission, due to the longer-cadence FFIs (1800 s and 600 s, respectively). The arrow in the top right panel indicates the flare observed in the afterglow of GRB 200412B.

An additional effect which can reduce the number of detected counts seen by TESS for GRBs is the onboard cosmic-ray rejection algorithm. This algorithm, described in detail in the Appendix, attempts to mitigate the impact of cosmic rays by removing outlier pixel values at the native 2 s CCD integration time, before they are coadded to create the FFIs. As a result, this procedure may affect observations of rapid variability on timescales of a few seconds. A full description of the TESS CRM technique is given in Section 5.1 of the TESS Instrument Handbook.[11] Typically, the fluence is underestimated by 20%–25% due to the effects of CRM; this value can be much larger for particularly bright bursts. However, for most bursts, CRM has no net effect on the calculated magnitude across the entirety of the exposure, as the increase in counts is roughly offset by the 25% increase in the exposure time.

In order to characterize the effect of TESS CRM on our sample of bursts, we compared the optical data to the high-energy light curve from Fermi-GBM and/or Swift-BAT under the assumption that the optical light curve has the same shape as the high-energy light curve.

2.4.1. High-energy Observations

We downloaded the data products available for the eight bursts of interest from the Fermi-GBM and Swift-BAT catalogs at NASA's High Energy Astrophysics Science Archive Research Center (HEASARC)[12]. For the Fermi data, we used the Time-Tagged Event (TTE) data from the single NaI detector with the highest signal-to-noise detection of the GRB. For Swift-BAT data (used to analyze GRBs 220623A and 230903A), we used the "Rate" light curves, which are sampled at 64 ms. All gamma-ray light curves were corrected for a constant background that was calculated from the data in the 100 s after gamma-ray emission activity ceased.

All binning and analyses were done using either the Fermi-GBM Data Tools (Goldstein et al. 2022), based on the Multi-Mission Maximum Likelihood framework (Vianello et al. 2015), or the `swift_too`[13] package.

2.4.2. Ensuring Consistency in the Time Systems

Light travel time effects between Fermi, Swift, and TESS make it imperative to ensure that the time systems are consistent when comparing data between these missions. We require 1 s accuracy on our light curves to compare Fermi and Swift light curves to individual frame readouts by TESS, which occur every 2 s. Given that the light travel time from TESS to the Earth can be up to 1.2 s at apogee, we corrected all time stamps to the JD – TDB time system (Eastman et al. 2010), using `astropy` to account for the light travel time to the solar system barycenter. For this analysis, we assumed that Fermi and Swift are located at the geocenter; these satellites are actually in low-Earth orbit, however, so this assumption introduces an ~23 ms error into our analysis. However, this discrepancy is small compared to the 1 s accuracy that is required to compare to the TESS FFIs.

To ensure an accurate barycentric correction for the TESS data at the time of trigger, we determined the exact position of TESS during the GRB using `SpiceyPy` (Annex et al. 2020), a Python wrapper to NASA's SPICE system (Acton 1996; Acton et al. 2018). The correction was then applied using the coordinates of the GRB, as derived from Swift-XRT. While there is a barycentric correction value provided as part of the FFIs produced by the Science Processing Operations Center pipeline (Jenkins et al. 2016), this value was unsuitable for our purposes, as this correction is calculated at the center of the field, which introduces a systematic error of a few seconds for sources that fall elsewhere on the detector.

We note that there may be some offset between the trigger times reported in BTJD and the times reported in Universal Time (UT), when converted to JD, throughout Section 3. This discrepancy primarily arises from the differing path lengths of light from the GRB to the Earth, where UT is measured, and to the solar system barycenter, where TDB is measured. Values for these corrections for the eight GRBs analyzed in this paper will be provided upon reasonable request to the corresponding author.

3. Optical Light-curve Analysis

For each of the eight GRBs with light curves in Figures 1 and 2, we analyzed the prompt emission and afterglow signatures in the TESS light curve. We first fit a broken power law to the observed afterglows (Beuermann et al. 1999; Li et al. 2012). We also fit single power laws to these afterglows, and chose the fit with the lower value of χ^2/degrees of freedom (dof). We fit data to the following functional forms, for a broken and single power law, respectively

$$F(t) = F_0\left[\left(\frac{t}{t_b}\right)^{\alpha_1\omega} + \left(\frac{t}{t_b}\right)^{\alpha_2\omega}\right] + B, \tag{5}$$

and

$$F(t) = F_0(t^{-\alpha_1}) + B. \tag{6}$$

Here, α_1 and α_2 are the power-law indices, t_b is the time of power-law steepening or turnover, ω is a smoothing parameter (that was held fixed at 10), F_0 is the flux normalization at t_b, or the amplitude of the single power law, and B is a nuisance parameter to marginalize over residuals in the background correction.

Table 3 reports the best-fit parameters for the GRBs where an afterglow could be modeled by either a single or a broken power law; in the case of GRB 200412B, we excluded all points that were visibly part of a flare. None of these power-law slopes are consistent with zero at the 1σ level. As part of our analysis of each GRB, we also characterized the effects of the TESS CRM strategy on the observed prompt optical flux, and established constraints on the "total" optical fluence (in counts) that would have been observed from each GRB had the CRM clipping not occurred. The results of our analysis of the prompt emission are reported in Table 4.

3.1. GRB 200412B

The Fermi Gamma-Ray Space Telescope triggered on this long GRB at 09:08:40 UT on 2020 April 12 (BTJD 1951.88161; Fermi GBM Team 2020). The fluence (10–1000 keV) was $8.00 \pm 0.04 \times 10^{-5}$ erg cm^{-2} (Mailyan et al. 2020). An afterglow was detected by Swift-XRT (Page et al. 2020); this afterglow fell within TESS's FOV for Sector 23, as well as the Northern Continuous Viewing Zone—it was observed from Sectors 14–26. Significant ground-based follow-up was performed by multiple observatories after the initial discovery of an optical transient by Lipunov et al. (2020a, 2020c); these observations were reported by Kumar et al. (2020b), Belkin et al. (2020), Moskvitin (2020), Ogawa et al. (2020), Stecklum et al. (2020), and Xin et al. (2020), among others. The measurements from the Devasthal Optical Telescope were published in Table 1 of Sagar et al. (2020).

---

[11] https://archive.stsci.edu/files/live/sites/mast/files/home/missions-and-data/active-missions/tess/_documents/TESS_Instrument_Handbook_v0.1.pdf

[12] https://heasarc.gsfc.nasa.gov/

[13] https://www.swift.psu.edu/too_api/index.php

Table 3
Best-fit Parameters for the Six Swift-XRT Gamma-Ray Bursts Detected by TESS Exhibiting a Clear Afterglow

Identifier	Power-law Type	F_0 (erg cm^{-2} s^{-1})	α_1	α_2	t_b (s)	Background (erg cm^{-2} s^{-1})	χ^2/dof
200412B	Broken	$1.18 \pm 0.07 \times 10^{-12}$	-0.89 ± 0.02	-1.79 ± 0.15	$3.93 \pm 0.16 \times 10^4$	$-8.13 \pm 3.63 \times 10^{-14}$	4.88
210204A	Broken	$1.04 \pm 0.09 \times 10^{-12}$	-0.37 ± 0.02	-1.18 ± 0.15	$2.03 \pm 0.19 \times 10^4$	$-1.62 \pm 0.38 \times 10^{-13}$	3.38
210504A	Broken	$5.16 \pm 0.53 \times 10^{-13}$	0.26 ± 0.13	-1.22 ± 0.26	$9.16 \pm 1.14 \times 10^3$	$-6.73 \pm 2.62 \times 10^{-14}$	3.23
230116D[a]	Single	$5.71 \pm 6.04 \times 10^{-12}$	-0.30 ± 0.29	⋯	⋯	$-2.69 \pm 6.40 \times 10^{-13}$	15.44
230307A	Broken	$1.96 \pm 0.37 \times 10^{-12}$	0.44 ± 0.12	-0.12 ± 0.03	$7.69 \pm 0.73 \times 10^3$	$-9.60 \pm 3.49 \times 10^{-13}$	4.01
230903A[a]	Single	$1.34 \pm 2.29 \times 10^{-9}$	-1.36 ± 0.30	⋯	⋯	$1.68 \pm 1.10 \times 10^{-14}$	2.63

Note. We fit power laws (broken and single, as in Equations (5) and (6), respectively) to the extinction-corrected light curves. The power-law type is indicated in the second column. We give the normalization F_0 (either the flux at t_b for a broken power law, or the normalization at 1 day postburst) and the power-law indices α_1 and α_2. The sixth column reports the break time t_b in seconds since the time of trigger (see Table 1). The "background" is a nuisance parameter that marginalizes over the residual errors in the background correction.

[a] Indicates light curves with F_0 consistent with 0.

Table 4
Fluxes, Fluences, and Cosmic-Ray Mitigation Corrections for the Five GRBs in Our Sample Exhibiting Significant Deviations from Zero Flux at the Time of Trigger That Could Be Consistent with Prompt Emission

Identifier	Observed Fluence in Prompt FFI (counts)	Total Observed Optical Fluence (counts)	Peak Observed Magnitude (TESS band)	Afterglow Contribution in Prompt FFI (counts)	Corrected Prompt Flux (counts)	Corrected $T_{\rm mag}$ of Prompt Emission
200412B	$2.95 \pm 0.01 \times 10^6$	$4.6 \pm 0.1 \times 10^6$	12.15 ± 0.05	$5.60 \pm 0.05 \times 10^5$	$4.50 \pm 0.10 \times 10^6$	5.7–11.5
200901A	$3.10 \pm 0.51 \times 10^3$	⋯	18.4 ± 0.3	⋯	$9.30 \pm 0.50 \times 10^3$	13.8–15.6
210204A	$3.83 \pm 0.07 \times 10^4$	$6.5 \pm 1.0 \times 10^5$	15.67 ± 0.05	$2.02 \pm 0.35 \times 10^4$	$2.13 \pm 0.20 \times 10^4$	14.6–16.5
220623A	$1.68 \pm 0.10 \times 10^4$	⋯	16.57 ± 0.07	⋯	$2.28 \pm 0.20 \times 10^4$	13.8–15.6
230307A	$3.74 \pm 0.03 \times 10^4$	$2.9 \pm 0.3 \times 10^5$	14.51 ± 0.05	⋯	$> 4.70 \pm 0.30 \times 10^4$	12.6–13.4
230903A	$3.03 \pm 0.30 \times 10^3$	⋯	17.20 ± 0.10	⋯	$3.85 \pm 0.40 \times 10^3$	12.5–16.8

Note. The second column is the observed fluence in counts, and the third column is the total observed burst fluence in TESS (from both prompt and afterglow emission). The fourth column is the estimated magnitude of the GRB at the time of trigger, calculated across the entire FFI exposure time. The fifth column is an estimate of the fluence from the afterglow in the FFI cadence spanning the time of trigger based on an extrapolation of the best-fit power law. The sixth column gives the corrected flux, by subtracting column (5) from column (2) and then correcting for the TESS CRM algorithm as described in the Appendix. The seventh column provides an estimated range for the magnitude of the prompt emission; this value is calculated using the burst's T_{90} as a lower limit for the emission duration, and the interval between the trigger time and the end of the contemporaneous FFI as the upper limit. We note that the Fermi telemetry limitations for GRB 230307A (Dalessi & Fermi GBM Team 2023) only allowed us to estimate a lower limit for the prompt optical flux. GRBs without a clear afterglow, or those where the afterglow did not contribute significantly to the flux in the FFI with prompt emission, are indicated by "..." in the relevant columns. We note there may be some contribution from a putative reverse shock to some of the values for the "prompt emission" flux and magnitude given in columns (2) and (4); this would overestimate the corrected flux in column (6).

3.1.1. The Light Curve

The emission from this GRB in TESS's band peaked at an apparent magnitude of 12.15 ± 0.05, and decayed over the following day (Figure 3); this burst also exhibited a flare between 1.5 and 2.1×10^4 s posttrigger. The peak extinction-corrected flux was $1.47 \pm 0.07 \times 10^{-10}$ erg cm^{-2} s^{-1}. This is approximately 50% lower than the peak estimate reported in Roxburgh et al. (2023), who used `tess-reduce` (Ridden-Harper et al. 2021) for their analysis. Part of this difference may be explained by the zero-point calculated by `tess-reduce`, which is 20.31 mag, instead of the value of 20.44 from the Instrument Handbook. A parallel analysis that we performed with `tess-reduce` yields a peak flux that is ~20% greater than our calculated value, which corresponds to a magnitude difference of 0.18. At this time, it is unclear why there exists a difference between the `tess-reduce` results and our values; a more detailed comparison of `tess-reduce` and our pipeline is given in Appendix A.2 of Fausnaugh et al. (2023b). In the interest of completeness, we also present (extinction-uncorrected) i-band measurements in Figure 3 that were reported by Ogawa et al. (2020) and Kumar et al. (2020a).

To fit the observed flare, we subtracted the best-fit broken power law for the afterglow from the data and fit a Gaussian, with a constant offset term, to the points corresponding to the flare. The best-fit parameters for the broken power-law fit to the TESS light curve are given in Table 3, and the parameters for the fit to the flare (peaking at ~17 ks postburst) are given in Table 5. The high χ^2/dof for the broken power law likely arises from outliers, such as the points near the power-law break, at $\sim 4 \times 10^4$ s postburst. Both fits—to the afterglow and the flare—are shown in Figure 3. The fits reported in Table 3 include all points except the flux in the FFI from the time at trigger, which deviates from the best-fit power law by over 7σ. Excluding the second point after the trigger (which shows a 2σ excess over the current best-fit broken power law) results in a marginally better fit. Given the timescale over which optical reverse shock emission occurs—hundreds of seconds (see, e.g., Figure 1 in Sari & Piran 1999b; Figure 3 in Yi et al. 2020)—we suggest that a reverse shock could plausibly explain some fraction of this observed flux excess. Additionally, excluding the second point from the fit yields $\alpha_2 = 1.79 \pm 0.15$, which is consistent with measurements at 1.5, 2.5, and 3.5 days from the Tautenburg Observatory to within 2σ. Those observations

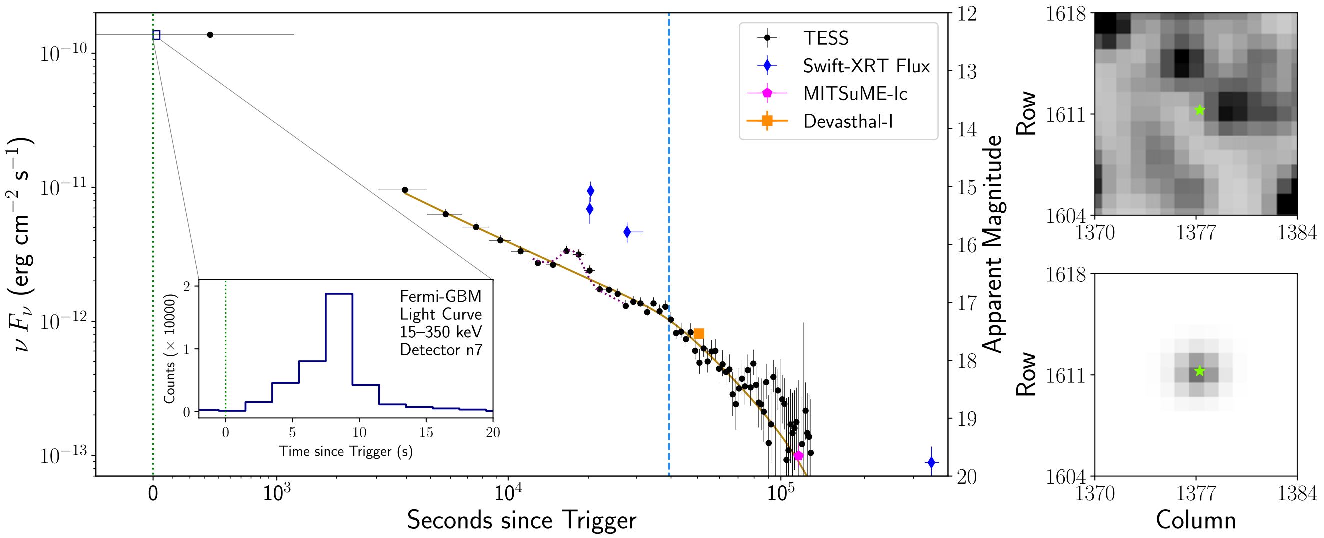

Figure 3. Left: the flux-calibrated, extinction-corrected TESS and Swift-XRT light curves of GRB 200412B. The x-axis measures the seconds since the time of Fermi-GBM trigger, indicated by a green dotted line. The best-fit broken power law for the afterglow is shown by the solid gold line. We also show a Gaussian fit to the flare with a purple dotted line. The vertical blue dashed line shows the break time t_b of the broken power-law fit. The Fermi-GBM light curve is shown in the inset, and the small blue rectangle shows the 20 s window expanded in the inset. We also include photometric measurements in the Cousins I band (Kumar et al. 2020a, orange square; Ogawa et al. 2020, pink pentagon). Right: the top panel shows the reference image for the GRB location (from Swift-XRT) in TESS Sector 23, while the bottom panel shows the difference image from the first point in the light curve; there is a clear point source at that position in the difference image. The green star indicates the location of the GRB from Swift-XRT. Reference images were created for each CCD in a sector by median stacking 20 FFIs with low backgrounds from throughout that sector (Fausnaugh et al. 2021).

Table 5
Best-fit Parameters, as in Table 3, for a Gaussian fit to the Flare in GRB 200412B

Parameter	Value
F_0 (erg s^{-1} cm^{-2})	$1.34 \pm 0.09 \times 10^{-12}$
Time of peak (s)	$1.79 \pm 0.01 \times 10^4$
Peak width (s)	$1.82 \pm 0.18 \times 10^3$
Background (erg s^{-1} cm^{-2})	$-3.02 \pm 0.86 \times 10^{-14}$

Note. This fit has a χ^2/dof of 8.7, likely due to the small number of points that were used.

yielded a decay slope of $\alpha = 1.582 \pm 0.004$ (Stecklum et al. 2020).

Swift-XRT observations of the afterglow concurrent with the TESS observation are also shown in Figure 3. Physical explanations for the observed break (at $\sim 4 \times 10^4$ s) are discussed further in Section 4.

3.1.2. The Prompt Emission

The GRB trigger occurred 561.51 s after the FFI starts, and the gamma-ray emission only lasted for a total of $\lesssim 20$ s (as seen in the inset in Figure 3). Thus, the observed flux in the 30 minute FFI that includes the time of trigger contains contributions from emission occurring on shorter timescales (internal or reverse shocks), as well as the afterglow. To quantify this effect, we extrapolate the afterglow power law to the approximate end of the prompt gamma-ray emission (600 s after the start of the FFI, or ~39 s after the trigger time) and calculate the fluence of the afterglow during this time, in counts; these values are listed in Table 4. We find that the afterglow contributes approximately 5.60×10^5 counts in this FFI (~20%). The remainder is shorter-timescale emission.

As described in the Appendix, we correct for the CRM within the two 20 s clipping intervals that span the entirety of the high-energy emission. We find that the CRM clips roughly 40% of the flux that would have been recorded as part of the prompt emission, as shown in Figure 11. Correcting for the clipped flux, we can constrain a range of values for the true magnitude of the prompt emission based on the emission duration. The lower limit for the duration of optical emission can be approximated by the T_{90} value, and the upper limit is the difference between the end of the FFI and the trigger time. This spans 3 orders of magnitude for this burst (6 to ~1250 s), so the magnitude is highly uncertain. We find that the prompt flash could have had a magnitude of anywhere from 5.7 to 11.5. In the 2 s exposure with the highest flux (which was clipped by the CRM), the instantaneous magnitude could have been as bright as 5.5 assuming that there is no reverse shock emission component in this FFI. However, if the shape of the prompt optical light curve deviates from that of the high- energy light curve, or the flux excess (partially) arises from a reverse shock, our flux corrections are systematically overestimated, and the magnitude of the prompt emission would actually be fainter than these estimates. The true value would then depend on the number of emission components and their relative strengths.

3.2. GRB 200901A

Swift-BAT triggered on this long GRB at 03:47:31 UT on 2020 September 1 (BTJD 2093.65995; Simpson et al. 2020). Using the Fermi-GBM data, Veres et al. (2020) reported a fluence in the 10–1000 keV band of $9.4 \pm 0.54 \times 10^{-6}$ erg cm^{-2}. The MASTER telescope network reported the detection of an optical transient at the Swift-XRT location 20 minutes after the trigger (Lipunov et al. 2020b), and the Swift Ultraviolet Optical Telescope (Swift-UVOT) reported a faint transient 50 minutes after the trigger (Breeveld et al. 2020).

The location of this GRB fell in TESS's FOV for Sector 29, and the light curve around the time of trigger is shown in Figure 1(b) and Figure 4. The trigger occurred ~140 s prior to the end of the TESS FFI. In this FFI, the optical magnitude is

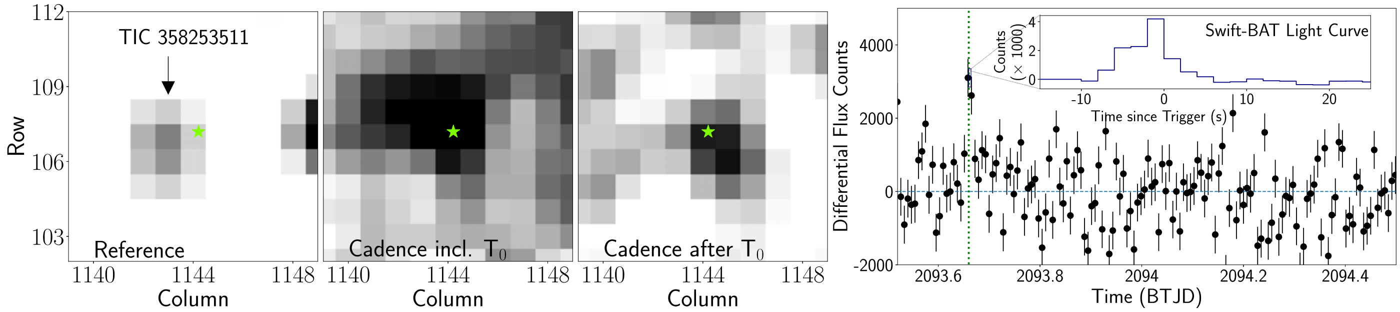

Figure 4. TESS images and light curve for GRB 200901A. The leftmost panel is the reference image at the location of the Swift-XRT localized afterglow; the next panel to the right is the difference image during the time of trigger; and the panel to the right of that is the difference image after the time of trigger, which shows some evidence for a source at that position. The light profile of the source at that location is distorted compared to the TESS PRF. The rightmost panel shows the TESS light curve, with the Swift-BAT light curve as an inset, and the trigger time marked by a dotted green line. The dashed blue line denotes zero flux. A potential contaminating star, discussed in Section 2.3, is labeled in the reference image.

$T = 18.4 \pm 0.3$; this detection is 3.8σ. There is also a 3.3σ flux excess in the subsequent FFI ($T = 18.6 \pm 0.3$). These magnitudes are consistent with the limit of $R \sim 17.8$ at 21.3 minutes postburst from Jelinek et al. (2020). Inspection of the difference image reveals a source at that location, although the light profile is somewhat distorted compared to the TESS pixel response function (PRF), as visible in Figure 4.

We used the Swift-BAT light curve to evaluate the effects of CRM on this burst. The trigger happened roughly in the middle of the emission, as visible in the inset of Figure 4—almost 102 s before the end of the FFI. The emission started approximately 110 s before the end of the FFI. We find that the CRM causes the fluence to be underestimated by around a factor of 3. The brightest 2 s optical flash might have had a magnitude of ∼11.8. Our estimated range for the corrected magnitude based on the T_{90} and the interval between the start of emission and the end of the FFI is 13.8–15.6.

3.3. GRB 210204A/AT2021buv

Fermi-GBM initially triggered on this long GRB at 06:29:25 UT on 2021 February 4 (BTJD 2249.77660; Fermi GBM Team 2021). The fluence was $5.76 \pm 0.04 \times 10^{-6}$ erg cm^{-2} in the 10–1000 keV band; its T_{90} of 206 s makes it the longest GRB in our sample with a confident detection in TESS. 45 minutes after the GRB trigger, the Zwicky Transient Facility (ZTF) independently triggered on an optical transient with magnitude $r = 17.11$, located within the Fermi localization region, as part of the Caltech–TESS shadowing survey (van Roestel et al. 2019). Swift also detected an uncatalogued X-ray source at the ZTF transient location (Kennea et al. 2021), further strengthening the association between this transient and the Fermi-GBM GRB. Xu et al. (2021a) reported a redshift of $z = 0.876$ using X-shooter at the Very Large Telescope. The results of significant multiwavelength follow-up are presented in Kumar et al. (2022), and light curves from radio to X-rays are shown in Figure 6 of their paper. The Fermi-GBM light curve is shown in the inset of our Figure 5, and the ZTF light curve of the afterglow is given in Figure 4 of Andreoni et al. (2021).

After performing the barycentric correction, we found that the prompt emission for this GRB lies wholly within a single 10 minute FFI cadence. The high-energy light curve exhibits four distinct peaks (labeled in the inset of Figure 5); Fermi triggered after the first. The gamma-ray peak with the highest fluence starts ∼160 s after the trigger. The FFI cadence with peak flux has a brightness of $T_{\rm mag} = 15.67 \pm 0.05$, without accounting for CRM.

As with GRB 200412B, we fit a broken power law to the light curve, both with and without the initial point (with maximum flux). The fits that include the first point are somewhat worse than those without this point, with $\chi^2/{\rm dof} \sim 3.74$. There may be comparable contributions from both the afterglow and prompt emission in this cadence. Additionally, there may be a plateau in the TESS light curve from 3 to 6×10^3 s posttrigger. Our power-law fits do not substantially change when including or excluding this feature, which suggests that this feature is statistically insignificant.

The best fit to the TESS data is shown in Figure 5, and the corresponding parameters are given in Table 3. We also jointly fit the TESS data and the *i*-band data from the observing log in Table A.1 of Kumar et al. (2022). This yields a revised estimate of $\alpha_2 = -0.76 \pm 0.04$, which is inconsistent with their results for the late-time power-law index. The time of the power-law break also shifted and became more uncertain, to $t_b = 8.7 \pm 2.1 \times 10^3$ s postburst. While $t_b \sim 0.1$ days is consistent with the weak constraint from Kumar et al. (2022, $t_b = 0.37 \pm 0.3$ days), the late-time decay index is not.

Given the presence of both a break in the TESS data, as well as another break observed by Kumar et al. (2022), we also evaluated whether a triple power-law fit to the data (Equations (2)–(4) in Li et al. 2012) was a better match to the observations. We find through the use of an *f*-test that this fit is marginally favored (at a ∼70% confidence level). The two breaks occur at $8.5 \pm 2.7 \times 10^3$ s postburst and $1.87 \pm 0.54 \times 10^5$ s postburst; the latter break occurs between the end of the TESS observations and the start of the Kumar et al. (2022) observations. The three power-law indices are $\alpha_1 = -0.33 \pm 0.05$, $\alpha_2 = -0.78 \pm 0.06$, and $\alpha_3 = -1.25 \pm 0.06$. The value for α_3 is consistent with the decay index found by Kumar et al. (2022) for the data at that time. Such a three-component power law could possibly be explained by early time energy injection, followed by a "normal" decay, and then a subsequent jet break (Zhang et al. 2006).

After removing contributions from the afterglow fluence in the TESS FFI (the afterglow was assumed to start at ∼300 s postburst, which marked the end of the gamma-ray emission in the Fermi-GBM light curve), we found that the CRM removes 15% of the prompt optical flux, under the assumption that it has the same shape as the high-energy light curve. We also calculated the magnitudes of the brightest 2 s optical flashes that would accompany each of the four peaks seen in the prompt emission, and found values of ∼16.15, 15.02, 13.20,

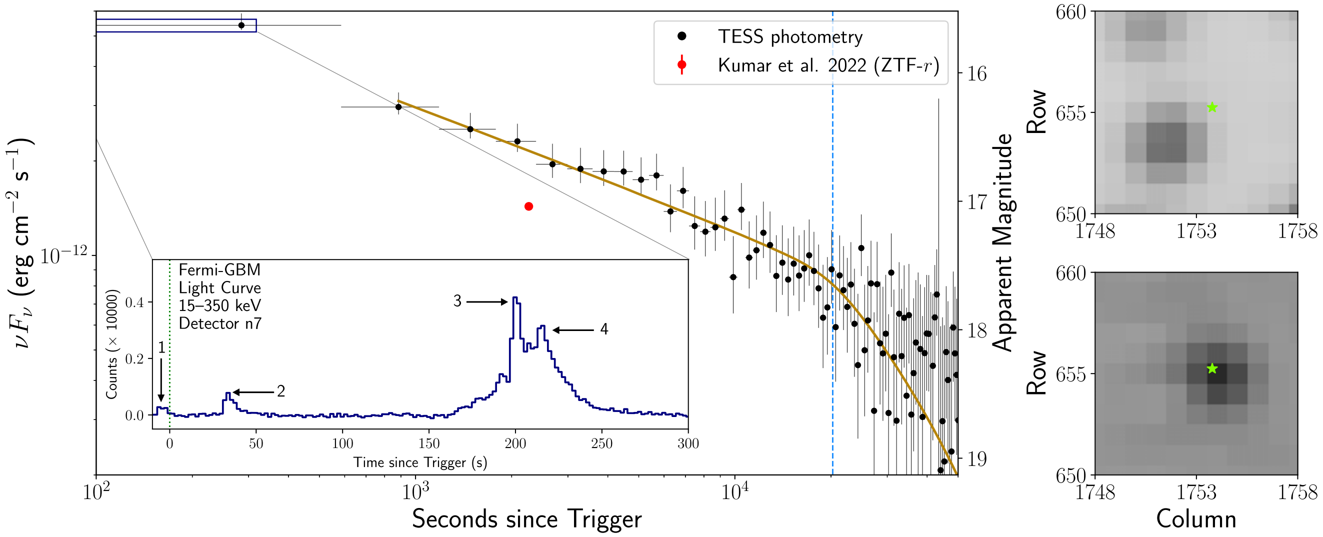

Figure 5. Same as Figure 3, but for GRB 210204A, including an extinction-corrected r-band afterglow measurement from Kumar et al. (2022) for comparison purposes (red dot). The four distinct peaks visible in the high-energy light curve are marked and numbered in the inset. The Swift-XRT light curve starts 10^5 s after the trigger time, at which point the afterglow had faded beyond the TESS detection limit, so it is not shown here. We find evidence for a temporal break at ∼21 ks postburst, but these points are close to TESS's detection limit, so the steepened power-law index is more uncertain. We do not show further observations from Kumar et al. (2022), who analyze data out to 10^6 s postburst; these data points would significantly affect the scale of this plot, so we direct the reader to their Figure 6 for the full light curve.

and 13.50. After these corrections, the magnitude of the optical prompt emission detected during the FFI was calculated to be 15.8, when integrated over the duration of the gamma-ray emission (∼300 s). However, since the duration of the prompt optical emission is uncertain, and could range from 100 to 600 s (the duration of the brightest peak to the duration of the FFI), this magnitude could range between 14.6 and 16.5.

Physical interpretations of the break seen in the TESS light curve are discussed in Section 4.2, as are the discrepancies between the TESS light curve and the predictions for the early time light curve from Kumar et al. (2022).

3.4. GRB 210504A

Swift-BAT detected the long GRB 210504A at 13:54:53 UTC on 2021 May 4 (BTJD 2339.08622; Lien et al. 2021); the X-ray afterglow was localized with the XRT, and fell within the TESS FOV for Sector 38. The fluence in the 15–150 keV band was $2.7 \pm 0.2 \times 10^{-6}$ erg cm^{-2} (Laha et al. 2021). The Nordic Optical Telescope detected an afterglow 9.3 hr postburst (Heintz et al. 2021), and Xu et al. (2021b) found $z = 2.077$ using X-shooter.

Visual inspection of the 10 minute cadence TESS light curve around the time of trigger revealed several points above zero flux that were consistent with the temporal profile of an afterglow rise and decay. There are formal 3σ detections of flux excesses in individual cadences approximately 2 hr after the trigger, which correspond to the cadences surrounding our best-fit afterglow peak time. There is also marginal evidence for a point source at the location of the burst in the FFI cadences after the trigger. The temporal coincidence between these measurements and the GRB trigger are consistent with an afterglow that peaks ∼9 ks after the burst. The best-fit parameters for the broken power law are enumerated in Table 3. Figure 6 shows both the original light curve and the light curve binned to 1800 s, and the best-fit broken power law for the afterglow.

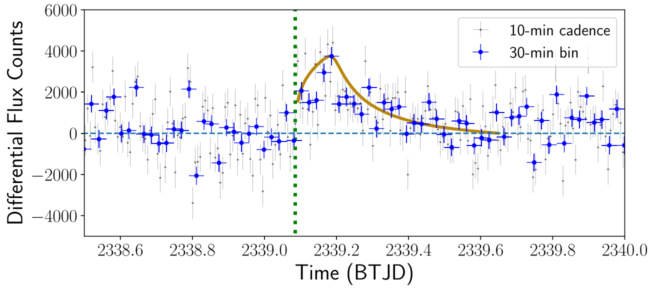

Figure 6. The light curve of GRB 210504A. The light gray points are the original light curve at 600 s cadence, and the blue points are the light curve binned to 1800 s. We also fit a broken power law to the 10 minute data and show the resulting fit in gold. This power law peaks at ∼9 ks postburst.

3.5. GRB 220623A

Swift-BAT triggered on this long-duration burst at 07:04:14 UT on 2022 June 23 (BTJD 2753.79238; Sbarufatti et al. 2022). The fluence was $3.5 \pm 0.1 \times 10^{-6}$ erg cm^{-2} in the 15–150 keV band (Parsotan et al. 2022). An optical counterpart detected 47 s after the trigger was reported by Hu et al. (2022); this was detected in a 1 s exposure from the BOOTES-5/Javier Gorosabel Telescope. An afterglow was detected in multiple 1 s exposures taken between the trigger and 30 minutes postburst, using the same telescope (Y.-D. Hu, 2024, private communication). The localized burst position fell within TESS's FOV for Sector 53.

We detected a 12.9σ deviation from zero flux in the 10 minute TESS cadence that spanned the time of the trigger (rightmost panel of Figure 7). Inspection of the difference images around the time of the trigger (second panel from left in Figure 7) reveals a point source in the FFI corresponding to the trigger time; this point source vanishes in the subsequent FFI. The flux in the FFI corresponds to an extinction-corrected $T_{\rm mag} = 16.57 \pm 0.07$. While these observations provide clear evidence for prompt optical emission, we do not find any indication of an accompanying afterglow. The lack of afterglow

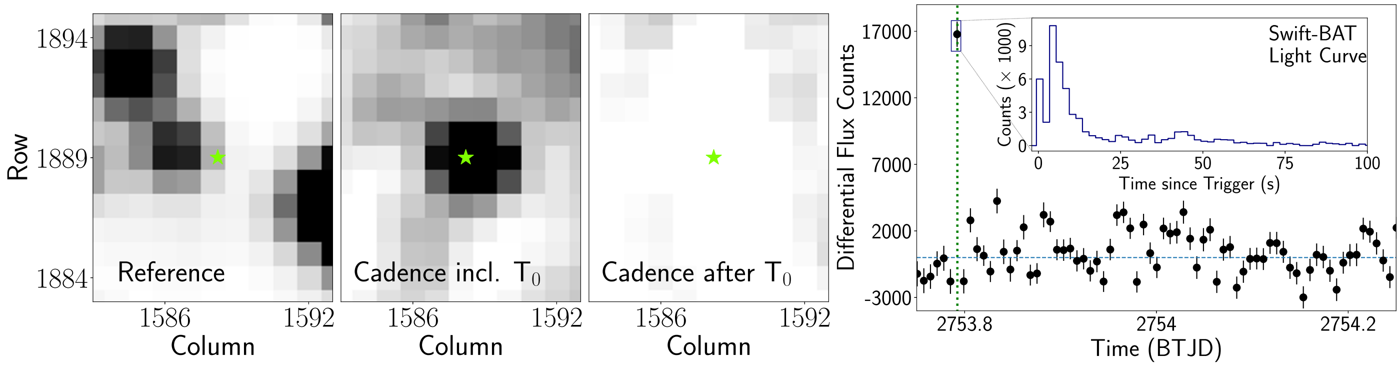

Figure 7. Same as Figure 4, but for GRB 230903A. There is a clear source in the difference image at the time of trigger, followed by a subsequent nondetection. The Swift-BAT light curve (inset) shows two distinct peaks, one of which likely is a precursor.

detection could be caused by the sky backgrounds in the FFIs during the 1.2 days before and after the trigger being large due to earthshine, and the afterglow likely being fainter than the 3σ detection limit of 18.16 in that sector.

After accounting for the effects of CRM, we find that it removes approximately 35% of the total flux. The gamma-ray emission has at least two distinct peaks (inset in the right panel of Figure 7), with other low-significance peaks starting 24 s after the trigger. The brightest 2 s optical flash has a magnitude of $\sim$12.2. Given the uncertainty in the optical emission duration (with a lower limit being the T_{90} of 50 s and an upper limit of 280 s, the interval between the trigger and the end of the exposure), our estimate for the true magnitude across the entirety of the prompt flash ranges from 13.8 to 15.6.

3.6. GRB 230116D

Swift-BAT triggered on this long burst at 21:04:43 UT on 2023 January 16 (BTJD 2961.38386; Sonbas et al. 2023). The measured fluence was $8.12 \pm 1.2 \times 10^{-7}$ erg cm^{-2} s^{-1} in the 15–150 keV band (Markwardt et al. 2023). Moskvitin et al. (2023a) found the burst's redshift to be $z = 3.81$ using the SCORPIO-2 spectrograph on the Special Astrophysical Observatory of the Russian Academy of Science telescope. The localized burst position fell within TESS's FOV for Sector 60. We find a 3σ deviation from zero flux around the time of trigger in the TESS data.

The peak flux in the 200 s cadence light curve corresponds to an extinction-corrected apparent magnitude of 17.71 ± 0.35, which is slightly above the 3σ detection limit of 17.84 given in Table 1. We fit the differential light curve to a single power law (shown in Figure 8, with the corresponding parameters in Table 3). The high χ^2/dof could be explained by the outliers present during the afterglow decay portion of the light curve. Moreover, the best-fit F_0 is consistent with zero. A statistical f-test, however, provides evidence (at a 95% confidence level) that the single power-law fit is favored over a fit to a constant flux. Given that there are three stars nearby with $G_{\mathrm{RP}} \sim 18$, noise from these stars could also induce significant scatter in the light curve before the GRB, which has the effect of making the detection limit brighter.

To verify our results from TESS data, we flux calibrated the early time r-band observation from Zhu et al. (2023), and found it to be consistent with the flux-calibrated TESS measurement. Additionally, we used the Rc-band photometry from 1 to 3 hr postburst reported in Moskvitin et al. (2023b) to verify the power-law index and some of the late-time detections visible in Figure 2(d)(ii). Combining the observation of Zhu et al. (2023) and the first observation of Moskvitin et al. (2023b), we find a decay slope of approximately -0.28, consistent with our result in Table 3. The Rc-band observations also show flaring behavior, with two distinct peaks; the peak of the first flare could explain one of the confident detections in Figure 2(d)(ii).

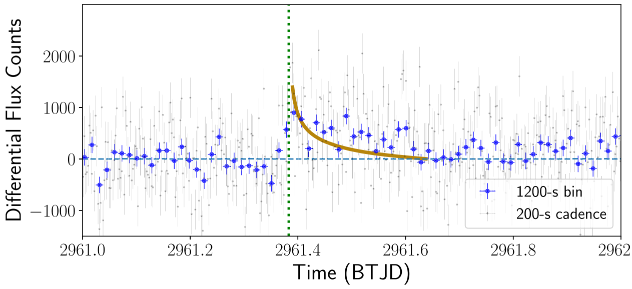

Figure 8. The light curve of GRB 230116D, as in Figure 6; here, the blue points are binned to 1200 s. The fit was performed with the original 200 s cadence data.

3.7. GRB 230307A

Fermi-GBM triggered on this long GRB at 15:44:06 UT on 2023 March 7 (BTJD 3011.15549; Fermi GBM Team 2023a). The measured fluence was $2.951 \pm 0.004 \times 10^{-3}$ erg cm^{-2} in the 10–1000 keV energy interval (Dalessi et al. 2023), which makes it one of the brightest bursts detected. An afterglow was clearly detected by Swift-XRT (Burrows et al. 2023), and the localized afterglow fell within TESS's FOV for Sector 62. The discovery of prompt optical emission with TESS and an accompanying afterglow was reported by Vanderspek et al. (2023) via GCN, and published by Fausnaugh et al. (2023a) and Levan et al. (2024a).

The TESS light curve displays a prompt emission component, followed by a rise and decay that likely correspond to an afterglow. Our best-fit values for the broken power-law fit to the afterglow are reported in Table 3; this is plotted in Figure 9. The prompt optical emission has a magnitude of $T = 14.51 \pm 0.05$.

For GRB 230307A, the prompt flash in the TESS light curve clearly precedes a distinct afterglow signal, so it seems reasonable to assume that the afterglow itself contributes negligible flux during the first 200 s TESS FFI cadence. Extrapolating the afterglow shows that its contribution accounts for $\lesssim$1% of the flux in the first FFI. Thus, we do not subtract any afterglow contribution when correcting for

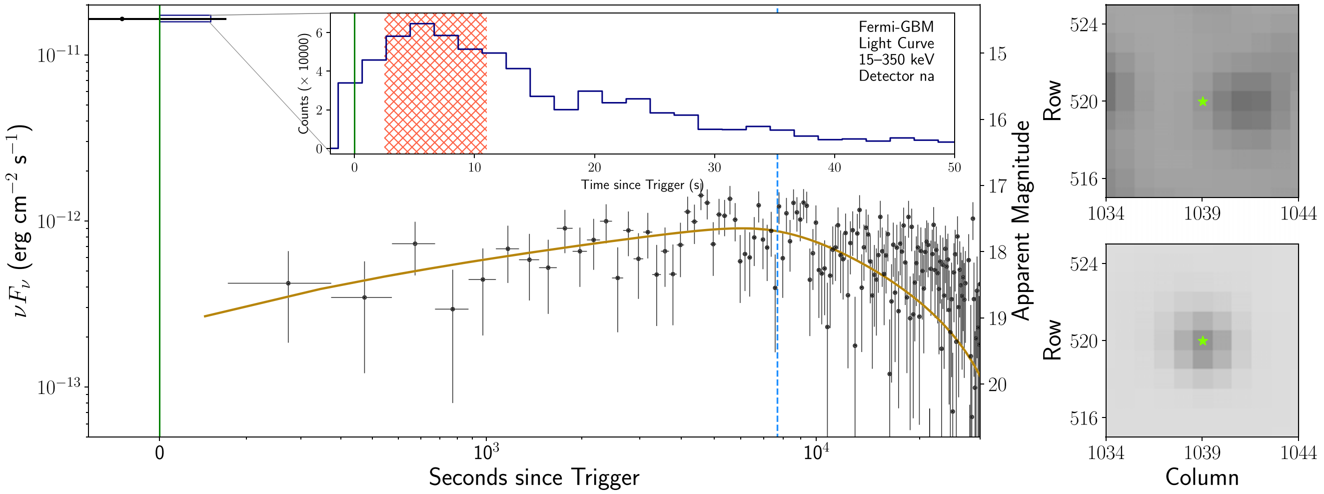

Figure 9. Same as Figures 3 and 5, but for GRB 230307A. In this case, the blue dashed line represents the peak time of the afterglow fitted by the break time parameter t_b in the broken power-law model. The Fermi-GBM TTE data from 2.5 to 11 s after the trigger are unreliable due to a pulse pileup issue, as described in Dalessi & Fermi GBM Team (2023); these times are marked by red cross-hatching in the inset Fermi-GBM light curve.

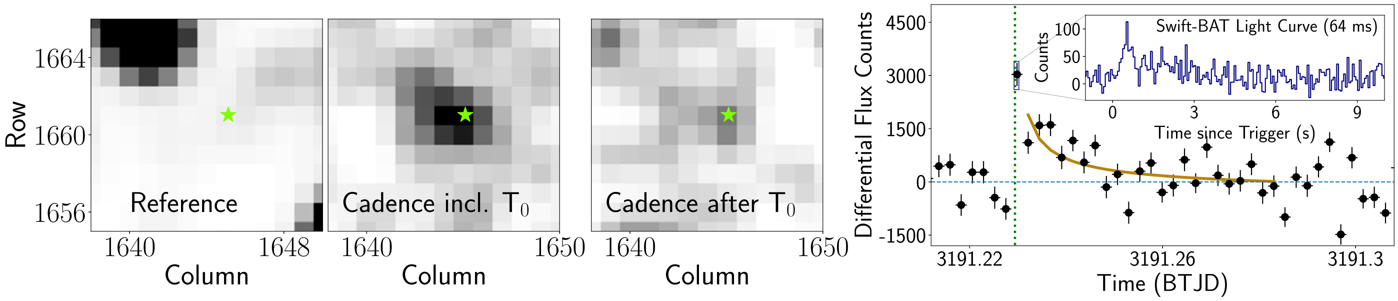

Figure 10. Same as Figure 4, but for GRB 230903A. The light profile of the GRB in the difference image has unusual structure that does not match the TESS PRF, but the temporal coincidence suggests that this is a counterpart to the GRB. The Swift-BAT light curve is shown at its native cadence of 64 ms to highlight the relatively short nature of the burst, compared to the other bursts in our sample. The best-fit single power-law model for the afterglow (parameters enumerated in Table 3) is shown in gold.

CRM. Because the Fermi-GBM TTE data from 2.5 to 11 s after the burst are unreliable due to limits on instrument telemetry (Dalessi & Fermi GBM Team 2023), our estimate for the corrected optical flux is only a lower limit. We find that the CRM algorithm clips ∼20% of the counts, which is almost exactly canceled by the 20% of exposure time removed and thus has no net effect on the reported magnitude.

We calculate the limits on the magnitude based on the T_{90} (35 s) and the interval between the trigger and the end of the FFI (72 s). We find a corrected magnitude range of 12.6–13.4 using the estimated prompt flux counts, after correcting for CRM. The brightest 2 s portion of the optical light curve had a magnitude of ∼12. Because the estimates for these magnitudes in the optical light curve were calculated based on the unreliable TTE data, these estimates are a lower limit on any correlated optical prompt emission and are likely fainter than the true magnitudes.

3.8. GRB 230903A

Both Fermi-GBM and Swift-BAT triggered on this intermediate-duration GRB ($T_{90} \sim 2.5$ s), with Fermi detecting the GRB at 17:22:58 UT (Fermi GBM Team 2023b), and Swift detecting this burst 2 s earlier (D'Ai et al. 2023). The time of the Swift-BAT trigger corresponds to BTJD 3191.22939. The fluence in the 15–150 keV band was $2.2 \pm 0.4 \times 10^{-7}$ erg cm^{-2} (Moss et al. 2023). This burst's spectrum suggests that it is an X-ray-rich burst, meaning that the ratio of the fluence in the 25–50 keV band to that in the 50–100 keV band is between 0.72 and 1.32 (Sakamoto et al. 2008). The localized burst position fell within the TESS FOV for Sector 69, and the discovery of prompt optical emission at this GRB's position was reported by Jayaraman et al. (2023).

We find that the prompt optical emission in the 200 s FFI cadence at the time of burst (using the Swift-BAT trigger time) has an apparent magnitude of $T = 17.2 \pm 0.1$ in the TESS band. While this cadence was the only point in the light curve to have a significant detection above the 3σ level ($T_{\rm mag} = 17.83$), we still fit a power law to the data from $t_0 + 100$ s (where t_0 is the time of trigger) to $t_0 + 5 \times 10^3$ s. We conducted a statistical f-test and found that a single power law was somewhat preferred (at an ∼99% confidence level) over a constant line. Including the first point (i.e., the prompt detection) in the fit results in a statistically indistinguishable fit, increasing the χ^2/dof by 0.01. The best-fit power law is shown in gold in the rightmost panel of Figure 10.

To evaluate the effects of CRM on the observed flux, we used the Swift-BAT light curve rather than the Fermi-GBM light curve due to (a) its more significant detection of the GRB, and (b) its finer time resolution. We do not include any afterglow contribution in the prompt FFI, because the extrapolation (from the model that excludes the first point) would lead to more flux than was actually observed at the time of trigger. The Swift-BAT trigger occurred 62.85 s after the start of the FFI, and there was only one episode of gamma-ray emission lasting approximately 2 s. We find that the TESS flux is underestimated by approximately 27% due to the effects of CRM. The brightest 2 s optical flash has a magnitude of $\sim$15.3.[14] Our estimated range for the true magnitude based on the T_{90}, and the interval between the trigger and the end of the FFI, is 12.5–16.8. This large range arises from the 135 s uncertainty in the duration of the optical emission.

4. Constraints on Physical Parameters

The TESS light curves of four GRBs from Section 3 provide enough information for us to constrain physical parameters of those bursts, including the initial Lorentz factor Γ_0 and the electron index p. Such an analysis is possible for GRBs 200412B, 210204A, 210504A, and 230307A. Where possible, we compare our derived constraints on Γ_0 and p to those available in the literature. In some cases, we utilize fiducial parameter values or values from the literature in our calculations.

4.1. GRB 200412B

From the light curve of GRB 200412B, we can constrain the initial bulk Lorentz factor Γ_0 and evaluate the potential physical mechanism underlying the observed power-law break in the light curve.

4.1.1. The Initial Bulk Lorentz Factor Γ_0

The time of afterglow peak indicates when the GRB fireball begins to decelerate, and the initial bulk Lorentz factor Γ_0 begins to change. Given that we do not observe a clear peak in the TESS light curve of this burst's afterglow (compare to GRB 230307A), we can infer that $t_{\rm peak} \lesssim 1200$ s—the amount of time between the trigger ($t = 0$) and the end of the FFI cadence spanning the initial emission. The expression for Γ_0, assuming a constant-density circumburst medium, is given in Sari & Piran (1999a) and Molinari et al. (2007)

$$\Gamma(t_{\rm peak}) = \left[\frac{3E_{\gamma,\rm iso}(1+z)^3}{32\pi n m_p c^5 \eta t_{\rm peak}^3}\right]^{\frac{1}{8}} \approx 160\left[\frac{E_{\gamma,\rm iso,53}(1+z)^3}{\eta_{0.2} n_0 t_{\rm peak,\,2}^3}\right]^{\frac{1}{8}}. \quad (7)$$

Here, $E_{\gamma,\rm iso} = 10^{53} E_{\gamma,\rm iso,53}$ is the isotropic energy released in gamma rays, $\eta = 0.2\eta_{0.2}$ is the radiative efficiency, $t_{\rm peak} = 100 t_{\rm peak,\,2}$ is the time of afterglow peak (in seconds), z is the redshift, n_0 is the particle density of the surrounding medium, and m_p is the proton mass. If we assume a fiducial GRB isotropic energy of 10^{53} erg, $\Gamma_0 = A \times (1+z)^{3/8}(\eta_{0.2} n_0)^{-1/8}$. Here, we have introduced a constant A that encapsulates estimates for $t_{\rm peak}$ ranging from 40 s postburst to 1200 s postburst (i.e., the end of the FFI cadence), without making assumptions about z, η, or n_0. Depending on the value of the peak time, A can range from 63 to 225, with a lower value for A corresponding to a later $t_{\rm peak}$. Identification of a host galaxy and spectroscopic measurements of its redshift can yield a revised estimate of Γ_0 that may better reflect the true value, given its comparatively weak dependence on $\eta_{0.2}$ and n_0.

The alternative model to a homogeneous circumburst medium is a wind medium, with a radial density power-law profile that can be written $n(r) = n_0 r^{-2}$. In this case, we must use a generalized version of Equation (7) (Nava et al. 2013; Ghirlanda et al. 2018) that introduces a power-law index s, which equals 2 in the wind case

$$\Gamma_0 = \left[\frac{(17-4s)(9-2s)3^{2-s}}{2^{10-2s}\pi(4-s)}\left(\frac{E_0}{n_0 m_p c^{5-s}}\right)\right]^{\frac{1}{8-2s}} t_{\rm p,z,2}^{-\frac{3-s}{8-2s}}. \quad (8)$$

Here,$t_{\rm p,\ z,2}$ is the redshift-corrected time normalized to 100 s ($t_{\rm p,2}/(1+z)$). For this case, the dependence on n_0 and z can be rewritten with a different constant B, which takes into account our fiducial value of $E_{\rm iso}$ and our range of $t_{\rm peak}$, and the normalization $n_0 \sim 10^{35}$ cm^{-1} given in Section 6 of Ghirlanda et al. (2018). We find that $\Gamma_{0,\rm wind} = B \times (1+z)^{1/4}$, with B ranging from 40 to 90 for our assumed values of $t_{\rm p}$. Lorentz factors for bursts with a wind medium must be lower than those for bursts occurring in homogeneous media. An empirical distribution of Lorentz factors for different circumburst media is shown in Figure 6 of Ghirlanda et al. (2018).

4.1.2. The Temporal Power-law Break

The clear change in the power-law decay slope observed in the light curve of GRB 200412B (blue dashed line in Figure 3) could arise from one of two physical phenomena. The first option is that this is the "jet break," a geometric effect wherein the jet has cooled and decelerated enough so that its relativistic beaming angle $1/\Gamma$ is greater than θ_j, the half-opening angle of the conical jet formed by the initial ejecta (Rhoads 1999). This value could be calculated if we were able to obtain constraints for z, $E_{\rm iso}$, n_0, and η. The other option is that the synchrotron cooling spectral break frequency ν_c is passing through the TESS bandpass, causing a steepening of the observed power-law slope; in this case, we can either constrain the circumburst density profile, or the temporal evolution of other burst parameters, like $E_{\rm iso}$ or the magnetic field fractional energy density ϵ_B.

The jet break is an achromatic effect, meaning that it should be visible in observations of the afterglow at all bands. There is no evidence for a break in the Swift-XRT light curve at the time of the observed break in TESS, as the late-time Swift-XRT observations (at $\sim$4 days postburst) agree with the power law from earlier times. Late-time observations (2 days postburst) from the Tautenburg Observatory (Klose et al. 2020) claim a steepening of the power-law decay that could be consistent with a jet break. However, these observations were only taken in one band (VB), and the purported time of jet break is not consistent with the available Swift-XRT data.

With earlier-time Swift-XRT data, we could also constrain the temporal evolution of the synchrotron cooling break frequency ν_c—assuming that the observed break in the light curve arises from ν_c passing through the TESS band. Sari

---

[14] While the T_{90} of this burst is only $\sim$2.5 s, the main gamma-ray emission was split over two 2 s TESS subexposures.

et al. (1998) predict that $\nu_c \propto t^{-0.5}$; however, significant deviations from this power law have been observed in several bursts (see, e.g., Racusin et al. 2008; Filgas et al. 2011). Decay slopes steeper than the canonical −0.5 could arise from either an accelerated stellar wind (which leads to a steeper, more negative power-law index in the $n(r)$ wind profile), or temporal evolution of the fractional magnetic energy density ϵ_B.

4.2. GRB 210204A

This GRB has been modeled and thoroughly analyzed in Kumar et al. (2022), and the best-fit physical parameters are reported in their Tables 1 and 2. The TESS light curve of this afterglow reveals tentative evidence for a temporal power-law break. As was done for GRB 200412B, we discuss the physical origin of this break (utilizing the best-fit parameters from the broken power-law fit, in the second row of Table 3), and attempt to determine whether this represents the synchrotron cooling break or the geometrical jet break. We also discuss new insights from the TESS data about this burst's afterglow.

4.2.1. The Temporal Power-law Break

For a constant-density circumburst medium, we utilize the power-law indices from Table 3 and the relationships for the interstellar medium (ISM) case from Table 1 of Zhang & Mészáros (2004) and Table 2 of Huang et al. (2005). This calculation yields electron indices of $p = 1.49 \pm 0.03$ and $p = 2.21 \pm 0.20$ when $\nu_c < \nu_{\rm TESS}$ and $\nu_c > \nu_{\rm TESS}$, respectively. For the wind case, we find that $p = 0.82 \pm 0.03$ and $p = 2.24 \pm 0.20$. Given that these two values must be consistent with each other before and after $\nu_c = \nu_{\rm TESS}$, the constant-density ISM case seems the most plausible, given that the early time and late-time indices have some overlap at the 3σ level. This may be a plausible interpretation, but our conclusion is low significance.

In order to evaluate the plausibility of the geometrical jet break interpretation (and constrain θ_j), we need a robust estimate for the circumburst density n, along with our best-fit value for t_b (Sari et al. 1999; Frail et al. 2001). However, the estimate provided by Kumar et al. (2022) for $\log_{10}(n_0) = -5.67$ appears relatively low compared to the typical values for n_0 for the GRBs presented in Table 2 of Panaitescu & Kumar (2002) and Table 1 of Yost et al. (2003). Such a low value for n_0 is more consistent with the comparatively less dense environments around short GRBs (Fong et al. 2015); GRB 210204A is not a member of this class of GRBs, given its extended emission. Modeling of the burst that incorporates the TESS data alongside the numerous measurements obtained by Kumar et al. (2022)—which is beyond the scope of this work—may revise this parameter to be more in line with those observed for long GRBs, and thereby robustly constrain θ_j.

4.2.2. The Overall Light Curve

Kumar et al. (2022) modeled the multiwavelength afterglow of GRB 210204A from radio to X-ray, and found that the r-band light curve should peak $\sim 4 \times 10^3$ s postburst (their Figure 7), when the synchrotron frequency ν_m passes through this bandpass. However, the TESS light curve does not show a peak at that predicted time. This discrepancy is likely explained by the fact that Kumar et al. (2022) have only one r-band data point at early times, leading to a poorly constrained early time light curve. The stark difference between their `afterglowpy` model and the TESS data highlights the degeneracies in afterglow modeling and the uncertainties introduced due to limited data. This example shows that TESS is able to provide crucial information about the early evolution of GRB afterglows; while multiwavelength follow-up was extremely useful in identifying late-time energy injection in this particular burst, characterizing the early afterglow is necessary to better constrain key burst parameters.

A potential explanation for the lack of an observed peak could be the presence of a relatively bright falling reverse shock occurring at times less than 4×10^3 s postburst—which would dominate over the afterglow rise before their estimated time of peak. As the afterglow rises and the reverse shock fades, the sum of these could produce the low-significance flattening seen in TESS.

4.3. Other Gamma-Ray Bursts: GRBs 210504A and 230307A

Given that we have best-fit estimates for the time of afterglow peak for GRBs 210504A and 230307A, we can qualitatively discuss the Lorentz factor Γ_0 for both.

For GRB 210504A, we also have a redshift value of $z = 2.077$ from X-shooter (Xu et al. 2021b), which corresponds to a luminosity distance of 16.6 Gpc;[15] utilizing the reported burst fluence from Laha et al. (2021) and our best-fit value for t_b yields an estimate for $E_{\rm iso}$ of 3×10^{52} erg. The late $t_{\rm peak}$—especially compared to that of GRB 200412B—suggests a lower Γ of around 40, implying the launching of a mildly relativistic jet.

We can perform a similar analysis for GRB 230307A, and compare the results to those published in Levan et al. (2024a). This burst is particularly interesting, as there is evidence that this GRB may arise from a binary neutron star merger at redshift $z = 0.065$, initially reported by Levan et al. (2023) and Bulla et al. (2023). Our results show a best-fit afterglow peak time of $\sim 7.7 \times 10^3$ s. If we adopt the isotropic energy value and circumburst densities from Levan et al. (2024a; $\log_{10}(E_{\rm iso}) = 51.29$, $\log_{10}(n_0) = -0.62$), and a fiducial $\eta_{0.2} = 1$ as in Molinari et al. (2007), we find a Lorentz factor of ∼25. Given this burst's distance from its purported host galaxy, we would expect a considerably less dense circumburst medium, with a density in line with the values in Table 4 of Fong et al. (2015); assuming $n_0 = 0.01$ cm^{-2} increases Γ_0 to 35. The difference between the two estimates for Γ_0 (ours and that from Levan et al. 2024a) is most likely attributable to our simplistic heuristic calculation, compared to their detailed multiwavelength physical modeling. However, their posterior distribution (Figure 12 in Levan et al. 2024a) provides relatively poor constraints on the value of Γ_0, and they also sampled Γ_0 in logarithmic space between 10^2 and 10^4. If this GRB were in fact located further away, in a higher-redshift galaxy at $z \sim 3.8$ (a possibility discussed in Levan et al. 2024a), it would have an $E_{\rm iso}$ of 10^{56} erg and $\Gamma_0 \sim 160$.

Another possibility is that the peak observed in the afterglow of GRB 230307A arises from other late-time central engine activity (such as a flare) rather than the forward shock of the afterglow itself. This would suggest that the real afterglow peak

---

[15] For this and all future calculations, we assume a typical Lambda cold dark matter (ΛCDM) cosmology (Planck Collaboration et al. 2020) as given in `astropy` (Astropy Collaboration et al. 2013, 2018, 2022), with $H_0 = 67.7$ km s^{-1} Mpc^{-1} and $\Omega_{\rm M} = 0.310$.

occurred between the end of the gamma-ray emission and the end of the FFI with prompt emission, implying a very rapidly rising and falling afterglow—so $t_{\rm peak} \lesssim 70$ s. For the nearby binary neutron star merger explanation, this would yield $\Gamma_0 \sim 140$; for a faraway collapsar, we find $\Gamma_0 \gtrsim 920$.

Finally, we highlight the similarity of this light curve to the optical emission associated with GRB 090727 (shown in Figure 2 of Kopač et al. 2013), where there is a sharp rise and fall at early times, followed by a more gradual rise and decay for the afterglow. In that case, Kopač et al. (2013) rule out a reverse external shock origin for the prompt flash and assert that it is likely caused by an internal shock, where the two colliding shells have very different Lorentz factors. However, their model does not require that the optical and gamma-ray emission originate from the same region; consequently, the two emission profiles would not necessarily be temporally correlated. This could suggest that the optical emission may arise a region such as the GRB photosphere, rather than from the jet.

TESS did not observe any features in the afterglows for these two bursts apart from the peak; the cooling and/or jet breaks likely occurred well after it faded beyond detectability, preventing us from meaningfully constraining p and θ_j.

5. Discussion

We have presented optical light curves for eight GRBs observed by TESS; these results demonstrate TESS's ability to obtain well-sampled, early time optical observations of GRBs. Prompt emission was clearly detected at the 3σ level in four GRBs in our sample, while a flux excess around the time of trigger that could be consistent with prompt or reverse shock emission was found in two of the other bursts. The TESS data also allow us to constrain key physical properties of the burst—including the Lorentz factor Γ_0 and the electron index p. Most importantly, observations with TESS come with no opportunity cost, unlike concerted ground-based target-of-opportunity follow-up campaigns. In this section, we estimate GRB detection rates in TESS and highlight the utility of TESS for GRB science.

5.1. Rate Estimates and Detectability

Given that the observed distribution of GRBs is isotropic on the sky (Briggs et al. 1996), and TESS observes a large fraction of the entire sky every 2 yr, we would expect many GRBs to fall into the TESS FOV. However, in practice, FOVs that include the Milky Way and/or periods of high scattered light will affect the rate of GRBs with a detectable signal in TESS.

Smith et al. (2021) predicted that TESS would be able to detect approximately one afterglow per year for GRBs that were also detected by high-energy monitors such as Fermi-GBM or Swift-BAT. This value is likely an underestimate, as TESS may observe previously unidentified optical afterglows for poorly localized GRBs. Here, we aim to estimate the number of concurrent detections between Swift-BAT and TESS. From the start of the TESS mission until the end of 2023 ($\sim$5.4 yr), there were 344 GRBs detected by BAT. This yields a detection rate of $\sim$64 yr^{-1}, which needs to be corrected by TESS's sky coverage (5.5%) and duty cycle (95%) in order to estimate the number of optical detections. From this calculation, we expect approximately 3–4 Swift-BAT GRBs per year to fall in the concurrent TESS FOV (roughly one every three sectors).

The previous calculation only accounts for Swift-BAT GRBs; however, there could be many more GRBs in the TESS FOV that were discovered by Fermi-GBM, which has a much larger effective FOV, but yields localizations that have uncertainties on the order of tens of square degrees. If we take the $\sim$1300 bursts observed by Fermi-GBM between 2018 July to 2023 September (using the `FERMIGBRST` catalog on HEASARC; Gruber et al. 2014; von Kienlin et al. 2014; Narayana Bhat et al. 2016; von Kienlin et al. 2020), we find that Fermi detects approximately 240 GRBs per year. Correcting this for the TESS FOV and duty cycle, we find that there could be 12–13 GRBs per year with localizations that overlap the concurrent TESS FOV, or approximately one per observing sector.

As part of our effort to rapidly identify GRBs falling in the TESS FOV, we have implemented a listener for Swift-BAT GCN Notices that will send us an alert whenever a well-localized GRB occurs within the contemporaneous TESS FOV. This code is based in part on the overlap tool from Mo et al. (2023). The rate estimates that we have calculated here appear to be roughly consistent with empirical observations—there were 22 GRBs from Swift-BAT, and 70 from Fermi-GBM, in the concurrent TESS FOV over the initial 5.4 yr of the mission, until 2023 December. We note that these estimates do not include GRBs that lack a high-energy trigger, such as the emerging class of "orphan afterglows" (see, e.g., Perley et al. 2024).

While these estimates are realistic, we note that not every GRB in the TESS FOV will yield a concurrent optical detection—we only had nine confident detections from our sample of 22 Swift-XRT bursts. The remaining 13 GRBs in our sample of 22 (i.e., those not discussed in Section 3) were likely not detected by TESS due to a combination of factors. For the specific case of GRB 210222B, which had multiple early time afterglow detections at $I \sim 16$ reported via GCN (e.g., Strausbaugh & Cucchiara 2021; Perley 2021), TESS did not detect it because it occurred during an observing gap. For GRB 190422A, the Galactic dust extinction was very high ($A_V \sim 4.3$), attenuating the flux by over a factor of 10 and likely playing a significant role in the nondetection. For other GRBs, the simplest explanation for the nondetections is that the prompt and afterglow emission peaked below the 3σ detection limits, as enumerated in Table 1.

5.2. Constraints on Late-time Emission

TESS's continuous monitoring of the sky allows us to establish constraints on late-time emission from GRBs. Supernova (SN) emission usually peaks $\gtrsim$20 days after the GRB (see, e.g., Galama et al. 1998; Klose et al. 2019). Kilonovae, on the other hand, manifest themselves just a few days after the trigger (see, e.g., Jin et al. 2015; Abbott et al. 2017), peaking in the TESS band at $\sim$1 day postburst (Figures 6 and 8 of Mo et al. 2023). If a GRB is sufficiently nearby and bright in TESS, and falls within the TESS FOV during the two sectors ($\sim$60 days) after the burst, we can place constraints on fainter late-time emission.

For all the GRBs in our sample, we visually searched light curves from 2 to 60 days after the burst and found no signals down a limiting magnitude of 18–19. Some of these nondetections were caused by either TESS's FOV in subsequent sectors shifting away from the burst's location, or a significant increase in backgrounds from scattered light due to the relative orientations of TESS, the Earth, and the Moon during its orbit.

We can establish a constraint on the redshift of GRB 200412B due to the lack of detection from any associated SN. Assuming that a putative GRB-SN is similar to SN 1998bw (associated with GRB 980425),[16] it would likely peak at an I-band absolute magnitude of ~ -19.2 (Galama et al. 1998). This assumption also agrees with the empirical distribution of GRB-SN absolute magnitudes from Richardson (2009). We binned the data from Sectors 24 and 25 to 6 hr due to the comparatively slow evolution of SNe, and to improve the 3σ detection limit to $\sim$20.5. Given our nondetection of any excess emission in Sectors 24 and 25—the two immediately following the burst— this means that any associated SN must have occurred further than $D_L = 870$ Mpc, so the GRB must have been located at $z > 0.18$. Other GRB-SNe have been found to peak at around -18 (Prentice et al. 2016); this value would weaken the distance constraint to $D_L \gtrsim 500$ Mpc ($z \gtrsim 0.11$).

5.3. Other Uses for TESS in Gamma-Ray Burst Science

TESS's excellent temporal coverage of GRB afterglows and its weekly downlink schedule will allow us to constrain physical parameters that could inform further multiwavelength follow-up efforts. As was shown in Section 4, we are able to estimate the initial bulk Lorentz factor Γ_0 from the afterglow peak. TESS observations can also identify afterglows with unusual behavior and inform further follow-up efforts through extrapolations of the observed power-law decay in order to predict the feasibility of planned observations. Conducting such analyses with TESS also does not rely on resource-intensive target-of-opportunity triggers for multiwavelength follow-up.

TESS can investigate the relationship of the prompt optical flux to the high-energy spectral energy distribution (SED; see, e.g., Figure 4 of Xin et al. 2023). An SED constraint from TESS at redder wavelengths would help distinguish between models for the optical flash, clarifying the relationship between the prompt high-energy and optical emission for a given GRB, including the emission region and mechanisms (R. Jayaraman et al. 2024, in preparation).

Finally, all searches in TESS for optical counterparts to GRBs have relied upon a concurrent high-energy detection by a GRB monitoring satellite such as Fermi-GBM or Swift-BAT. However, TESS may also be able to detect so-called "orphan afterglows" (which lack a corresponding gamma-ray trigger) and "dirty fireballs" (transients whose relativistic ejecta has too many baryons to produce a GRB). Recently, Perley et al. (2024) were able to utilize TESS data to constrain the time of explosion of the fast relativistic transient AT2019pim and establish stringent limits on the detectability of possible gamma-ray emission from this transient. The detection of more fast relativistic transients in TESS via a blind search (R. Jayaraman et al. 2024, in preparation) could trigger timely multiwavelength follow-up, especially with the current cadence of weekly downlinks.

6. Conclusions and Future Work

In this work, we present TESS light curves of eight well-localized GRBs with evidence for prompt optical and/or afterglow emission. We constrain physical parameters for four of these bursts using TESS light curves, and account for the TESS CRM strategy in order to constrain the brightness of any associated prompt optical flashes. We also briefly discuss the possibilities for TESS to detect late-time emission from GRBs, and highlight that it is one of the few observatories capable of detecting both prompt and afterglow emission from GRBs.

Modifications to TESS's operations during its Extended Mission 2 have enhanced its ability to detect and disseminate information about observations of prompt optical emission more rapidly, as well as significantly improved our ability to distinguish between prompt and afterglow emission—particularly in the case of GRB 230307A. Moreover, given that the weekly downlink schedule now enables the rapid creation and public dissemination of the TICA FFIs, we are able to identify GRB signatures in TESS within days—considerably earlier than in previous phases of the mission.

We also note that TESS's large sky coverage, combined with the isotropic distribution of GRBs on the sky, means that there will be at least a few GRBs discovered in TESS's FOV each year. This detection rate is aided by the fact that TESS has limited downtime—it is neither subject to the constraints of ground-based observatories (e.g., day–night cycles and weather), nor those of space-based observatories in low-Earth orbit (e.g., Earth occultation and the South Atlantic Anomaly).[17]

Given our predicted rate of up to 10 detections per year of optical counterparts to GRBs in TESS, we can expect to identify many more as the mission proceeds. We also plan to utilize TESS to follow up on GRBs and other relativistic fast transients detected by the recently launched Einstein Probe (Yuan et al. 2018, 2022), which is sensitive to GRBs throughout a larger parameter space, including at higher redshift and in softer bands (e.g., Levan et al. 2024b; Liu et al. 2024). The recently launched Space Variable Objects Monitor (Wei et al. 2016) will also significantly increase the number of GRBs detected and rapidly localized. TESS clearly fulfills a unique role in detecting and characterizing GRBs, and will serve as a useful complement to other optical large-scale surveys, such as ZTF (Bellm et al. 2019) and the upcoming Legacy Survey of Space and Time at the Vera Rubin Observatory (Ivezić et al. 2019).

Acknowledgments

We thank the anonymous referee for the comments and feedback, which greatly strengthened the resulting paper. The authors thank Youdong Hu for information about BOOTES observations of the afterglow of GRB 220623A. R.J. also thanks Frédéric Daigne for insightful discussions about models for GRB prompt and precursor emission, Jochen Greiner for information about GRB catalogs, and Te Han for discussions regarding photometric techniques to correct for contaminated sources.

The authors would also like to thank the staff at the Mikulski Archive for Space Telescopes (MAST), especially Hannah Lewis, Julie Imig, Travis Berger, and Scott Fleming, who assist

---

[16] This assumption is fairly common in studies of GRB-SNe; see, e.g., Srinivasaragavan et al. (2023).

[17] TESS is in a unique, elliptical high-earth orbit that places it in a 2:1 resonance with the Moon.

with the rapid ingest and dissemination of the early release TICA data products.

This paper includes data collected by the TESS mission. Funding for TESS is provided by the NASA Explorer Program. The TICA data used in this work was obtained from MAST (doi:10.17909/t9-9j8c-7d30), hosted by the Space Telescope Science Institute (STScI). STScI is operated by the Association of Universities for Research in Astronomy, Inc., under NASA contract NAS 5-26555.

This work has made use of data from the UK Swift Science Data Center at the University of Leicester; Swift and Fermi data provided by the High Energy Astrophysics Science Archive Research Center (HEASARC), a service of the Astrophysics Science Division at NASA/GSFC; and data from the NASA/IPAC Extragalactic Database (IRSA 2022), which is funded by the National Aeronautics and Space Administration and operated by the California Institute of Technology.

Facilities: TESS, Swift, Fermi.

Software: `astropy` (Astropy Collaboration et al. 2013, 2018, 2022), `lightkurve` (Lightkurve Collaboration et al. 2018), `matplotlib` (Hunter 2007), `numpy` (Harris et al. 2020), `scipy` (Virtanen et al. 2020), `tess-reduce` (Ridden-Harper et al. 2021), Fermi-GBM Data Tools (Goldstein et al. 2022), SpiceyPy/SPICE (Acton 1996; Acton et al. 2018; Annex et al. 2020), `swift_too` (https://www.swift.psu.edu/too_api/), and `synphot` (STScI Development Team 2018)

Appendix
Accounting for Cosmic-Ray Mitigation in TESS

The TESS detectors read out every 2.0 s. In order to construct an FFI, TESS coadds these 2 s exposures to reach the full cadence of 200 s, 600 s, or 1800 s. Cosmic rays are rejected during this coadding process as follows: The two-second images are examined in sets of 10 (corresponding to a 20 s time interval), and the highest and lowest values for each pixel are discarded, and the remaining eight values are summed. The effective exposure time is reduced by 20%, but the effect of cosmic rays is significantly mitigated. Further information about the CRM can be found in Section 5.1 of the TESS Instrument Handbook (https://archive.stsci.edu/files/live/sites/mast/files/home/missions-and-data/active-missions/tess/_documents/TESS_Instrument_Handbook_v0.1.pdf).

This procedure also affects astrophysical signals that vary on timescales of 10 s or less, such as the prompt optical emission from GRBs. In these cases, TESS's CRM strategy could remove 2 s cadences that contain signals from the prompt GRB emission, leading to an underestimate of the total burst fluence.

We estimated the effect of the TESS CRM technique on the observed optical flux from the GRBs in our sample, in order to constrain the brightness of any prompt optical emission. This portion of our analysis relies upon the assumption that the high-energy light curve (from 15 to 350 keV) is correlated with the observed prompt optical light curve; this behavior was observed by Vestrand et al. (2005), Racusin et al. (2008), Vestrand et al. (2014), and a subset of the sample of GRBs presented in Oganesyan et al. (2019). It has also been suggested that both the optical and gamma-ray emission may originate from a common region (Racusin et al. 2008). However, other studies (e.g., Sari & Piran 1999b; Klotz et al. 2006; Yost et al. 2007; Gruber et al. 2011) did not find such a correlation between the optical emission and the high-energy prompt emission. Whether or not such a correlation exists, the fluence detected by TESS for any prompt counterpart would still represent a lower limit, due to the CRM strategy removing flux. The effect of TESS CRM is even larger if the prompt optical emission consists of several peaks and spans multiple 20 s clipping bins, as there will be two or more clipped peaks throughout the period of extended emission. This could have occurred in the detection of prompt emission for GRB 210204A, where the emission lasted for hundreds of seconds.

Figure 11 provides a visual representation of how we account for the onboard CRM algorithm. For this analysis, we assumed the optical prompt emission matched the light curves in the 15–350 keV band; this matches the energy regimes from Vestrand et al. (2014), Racusin et al. (2008), and Vestrand et al. (2005). First, we calculated the times of the TESS 2 s subexposures and the 20 s clipping blocks using the `TSTART` and `TSTOP` header keywords in the FFIs after correcting to the solar system barycenter, as described in Section 2.4.2. We then rebinned the high-energy light curve into these 2 s bins, and discarded the highest and lowest flux values within each 20 s block. Next, we integrated the remaining light curve and rescaled it so that the total counts matched the observed counts from the TESS light curve. Then, we added back in the clipped bins from the high-energy light curve, rescaled to match the TESS flux scale. Finally, we recalculated the observed magnitude using the corrected counts within various relevant timescales—the 2 s readout, the duration of the GRB (as approximated by T_{90}), and the native FFI cadence for that particular sector. These updated values are given in magnitudes in the discussion for each GRB in Section 3, and in counts in Table 4.

This strategy for handling CRM relies on the assumption that the clipped bins are the same for each pixel that has a signal from the GRB. The clipped bins may not be the same for all the pixels within the photometric aperture. However, the source counts per pixel near the core of the point-spread function (PSF) is 10 times larger than the total noise per pixel for the faintest prompt detection in our sample, GRB 230903A. Because the wings of the PSF contribute little to the integrated flux, assuming that the clipped bins are the same for each pixel for the optical flash is reasonable.

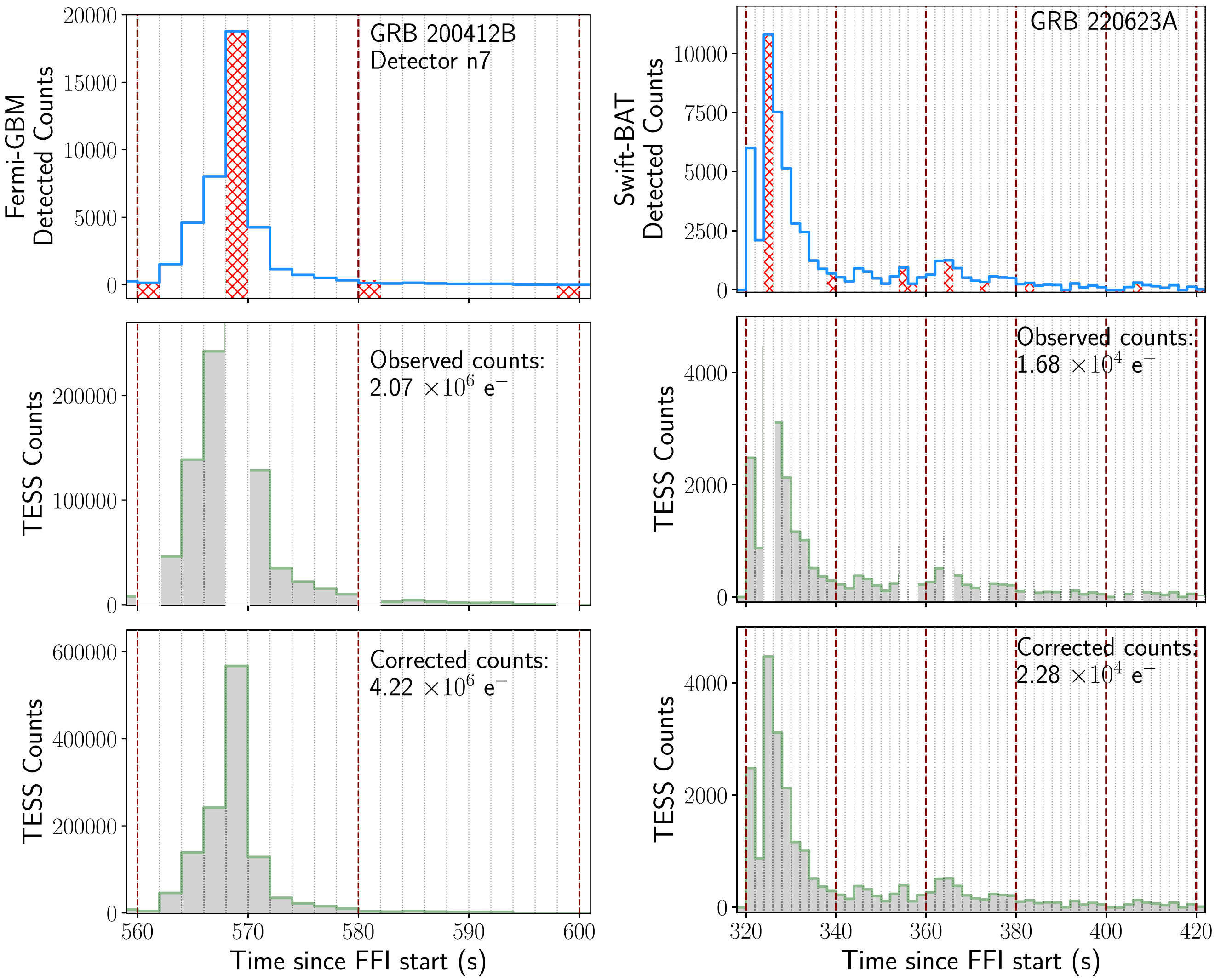

Figure 11. Visual representation of our CRM strategy, as applied to GRBs 200412B and 220623A. The latter has just a prompt detection in TESS, while the former has an afterglow and a likely prompt component detected (see Section 3 for details). We assume that the prompt optical flux tracks the high-energy flux, as in Vestrand et al. (2005, 2014) and Racusin et al. (2008). The dotted lines show the 2 s TESS subexposure boundaries, and the thicker maroon dashed lines show the 20 s CRM clipping intervals (see the Appendix text for details). Top: the Fermi-GBM light curve at 15–350 keV for GRB 200412B (left), and the Swift-BAT light curve at 15–350 keV for GRB 220623A (right), binned to the 2 s TESS exposures for the FFI during the prompt emission. The red cross-hatching signifies the times of maximum and minimum detected counts in each 20 s interval. Assuming the optical flux matches the gamma-ray light curve, these intervals would be clipped by the TESS CRM algorithm. Middle: the high-energy light curve, scaled to match the observed TESS counts. The cadences with the maximum and minimum number of detected counts for each 20 s interval are masked. The shaded gray area integrates to the total number of counts from the TESS light curve (annotation at the upper right). For GRB 200412B, this value has been corrected for the extrapolated afterglow contribution. Bottom: the TESS light curve for both bursts, with the clipped intervals reinserted. Over half the optical flux may have been clipped for GRB 200412B, while ∼25% was clipped for GRB 220623A.

ORCID iDs

Rahul Jayaraman https://orcid.org/0000-0002-7778-3117
Michael Fausnaugh https://orcid.org/0000-0002-9113-7162
George R. Ricker https://orcid.org/0000-0003-2058-6662
Roland Vanderspek https://orcid.org/0000-0001-6763-6562
Geoffrey Mo https://orcid.org/0000-0001-6331-112X

References

Abbott, B. P., Abbott, R., Abbott, T. D., et al. 2017, ApJL, 848, L12
Acton, C., Bachman, N., Semenov, B., & Wright, E. 2018, P&SS, 150, 9
Acton, C. H. 1996, P&SS, 44, 65
Akerlof, C., Balsano, R., Barthelmy, S., et al. 1999, Natur, 398, 400
Alard, C., & Lupton, R. H. 1998, ApJ, 503, 325
Andreoni, I., Coughlin, M. W., Kool, E. C., et al. 2021, ApJ, 918, 63
Annex, A., Pearson, B., Seignovert, B., et al. 2020, JOSS, 5, 2050
Astropy Collaboration, Price-Whelan, A. M., Lim, P. L., et al. 2022, ApJ, 935, 167
Astropy Collaboration, Price-Whelan, A. M., Sipőcz, B. M., et al. 2018, AJ, 156, 123
Astropy Collaboration, Robitaille, T. P., Tollerud, E. J., et al. 2013, A&A, 558, A33
Atwood, W. B., Abdo, A. A., Ackermann, M., et al. 2009, ApJ, 697, 1071
Barthelmy, S. D., Cummings, J. R., Gropp, J. D., et al. 2019, GCN, 26012
Barthelmy, S. D., D'Elia, Krimm, H. A., et al. 2022, GCN, 32361
Becerra, R. L., De Colle, F., Cantó, J., et al. 2021, ApJ, 908, 39
Belkin, S., Pozanenko, A., Shein, A. V., et al. 2020, GCN, 27604
Bellm, E. C., Kulkarni, S. R., Graham, M. J., et al. 2019, PASP, 131, 018002
Beloborodov, A. M., Hascoët, R., & Vurm, I. 2014, ApJ, 788, 36
Berger, E. 2014, ARA&A, 52, 43
Beuermann, K., Hessman, F. V., Reinsch, K., et al. 1999, A&A, 352, L26
Blake, C., & Bloom, J. S. 2004, ApJ, 606, 1019
Blake, C. H., Bloom, J. S., Starr, D. L., et al. 2005, Natur, 435, 181
Bloom, J. S., Starr, D. L., Blake, C. H., Skrutskie, M. F., & Falco, E. E. 2006, in ASP Conf. Ser. 351, Astronomical Data Analysis Software and Systems XV, ed. C. Gabriel et al. (San Francisco, CA: ASP), 751
Bohlin, R. C. 2014, AJ, 147, 127
Breeveld, A. A., Simpson, K. K. & Swift/UVOT Team 2020, GCN, 28342

Briggs, M. S., Paciesas, W. S., Pendleton, G. N., et al. 1996, ApJ, 459, 40
Bulla, M., Camisasca, A. E., Guidorzi, C., et al. 2023, GCN, 33578
Burd, A., Cwiok, M., Czyrkowski, H., et al. 2005, NewA, 10, 409
Burlon, D., Ghirlanda, G., Ghisellini, G., et al. 2008, ApJL, 685, L19
Burrows, D. N., Gropp, J. D., Osborne, J. P., et al. 2023, GCN, 33465
Cano, Z., Wang, S.-Q., Dai, Z.-G., & Wu, X.-F. 2017, AdAst, 2017, 8929054
Cardelli, J. A., Clayton, G. C., & Mathis, J. S. 1989, ApJ, 345, 245
Coppin, P., de Vries, K. D., & van Eijndhoven, N. 2020, PhRvD, 102, 103014
D'Ai, A., Ambrosi, E., Gropp, J. D., et al. 2023, GCN, 34601
Dalessi, S. & Fermi GBM Team 2023, GCN, 33551
Dalessi, S., Roberts, O. J., Meegan, C. & Fermi GBM Team 2023, GCN, 33411
Eastman, J., Siverd, R., & Gaudi, B. S. 2010, PASP, 122, 935
Eichler, D., Livio, M., Piran, T., & Schramm, D. N. 1989, Natur, 340, 126
Evans, P. A., Beardmore, A. P., Page, K. L., et al. 2009, MNRAS, 397, 1177
Fausnaugh, M. M., Burke, C. J., Ricker, G. R., & Vanderspek, R. 2020, RNAAS, 4, 251
Fausnaugh, M. M., Jayaraman, R., Vanderspek, R., et al. 2023a, RNAAS, 7, 56
Fausnaugh, M. M., Vallely, P. J., Kochanek, C. S., et al. 2021, ApJ, 908, 51
Fausnaugh, M. M., Vallely, P. J., Tucker, M. A., et al. 2023b, ApJ, 956, 108
Fermi GBM Team 2020, GCN, 27547
Fermi GBM Team 2021, GCN, 29390
Fermi GBM Team 2023a, GCN, 33405
Fermi GBM Team 2023b, GCN, 34608
Feroci, M., Frontera, F., Costa, E., et al. 1997, Proc. SPIE, 3114, 186
Filgas, R., Greiner, J., Schady, P., et al. 2011, A&A, 535, A57
Fong, W., Berger, E., Margutti, R., & Zauderer, B. A. 2015, ApJ, 815, 102
Frail, D. A., Kulkarni, S. R., Sari, R., et al. 2001, ApJL, 562, L55
Galama, T. J., Vreeswijk, P. M., van Paradijs, J., et al. 1998, Natur, 395, 670
Gehrels, N., Chincarini, G., Giommi, P., et al. 2004, ApJ, 611, 1005
Gendre, B., Stratta, G., Atteia, J. L., et al. 2013, ApJ, 766, 30
Ghirlanda, G., Nappo, F., Ghisellini, G., et al. 2018, A&A, 609, A112
Goad, M. R., Tyler, L. G., Beardmore, A. P., et al. 2007, A&A, 476, 1401
Goldstein, A., Cleveland, W. H., Kocevski, D., et al. 2022, Fermi GBM Data Tools: v1.1.1, https://fermi.gsfc.nasa.gov/ssc/data/analysis/gbm
Gruber, D., Goldstein, A., Weller von Ahlefeld, V., et al. 2014, ApJS, 211, 12
Gruber, D., Krühler, T., Foley, S., et al. 2011, A&A, 528, A15
Harris, C. R., Millman, K. J., van der Walt, S. J., et al. 2020, Natur, 585, 357
Heintz, K. E., Perley, D. A., Malesani, D. B., & Djupvik, A. A. 2021, GCN, 29937
Ho, A. Y. Q., Perley, D. A., Yao, Y., et al. 2022, ApJ, 938, 85
Hu, Y. D., Fernandez-Garcia, E., Caballero-Garcia, A. J. C.-T. M. D., et al. 2021, GCN, 29546
Hu, Y. D., Fernandez-Garcia, E., Perez-Garcia, I., et al. 2022, GCN, 32251
Huang, K. Y., Urata, Y., Filippenko, A. V., et al. 2005, ApJL, 628, L93
Hunter, J. D. 2007, CSE, 9, 90
IRSA 2022, Galactic Dust Reddening and Extinction, IPAC, doi:10.26131/IRSA537
Jayaraman, R., Fausnaugh, M. M., Vanderspek, R., & Ricker, G. R. 2023, GCN, 34650
Jelinek, M., Strobl, J., Masek, M., et al. 2020, GCN, 28767
Jenkins, J. M., Twicken, J. D., McCauliff, S., et al. 2016, Proc. SPIE, 9913, 99133E
Jin, Z.-P., Li, X., Cano, Z., et al. 2015, ApJL, 811, L22
Ivezić, Ž., Kahn, S. M., Tyson, J. A., et al. 2019, ApJ, 873, 111
Kennea, J. A., Osborne, J. P., Page, K. L., et al. 2021, GCN, 29431
Klebesadel, R. W., Strong, I. B., & Olson, R. A. 1973, ApJL, 182, L85
Klose, S., Schmidl, S., Kann, D. A., et al. 2019, A&A, 622, A138
Klose, S., Stecklum, B., Melnikov, S., & Nicuesa Guelbenzu, A. 2020, GCN, 27593
Klotz, A., Boër, M., Atteia, J. L., & Gendre, B. 2009, AJ, 137, 4100
Klotz, A., Gendre, B., Stratta, G., et al. 2006, A&A, 451, L39
Kobayashi, S. 2000, ApJ, 545, 807
Kopač, D., Kobayashi, S., Gomboc, A., et al. 2013, ApJ, 772, 73
Koshut, T. M., Kouveliotou, C., Paciesas, W. S., et al. 1995, ApJ, 452, 145
Kouveliotou, C., Meegan, C. A., Fishman, G. J., et al. 1993, ApJL, 413, L101
Krimm, H. A., Barthelmy, S. D., Cummings, J. R., et al. 2019, GCN, 24941
Krimm, H. A., Barthelmy, S. D., Laha, S., et al. 2022, GCN, 37811
Kumar, A., Aryan, A., Pandey, S. B., et al. 2020a, GCN, 27564
Kumar, A., Pandey, S. B., Aryan, A., et al. 2020b, GCN, 27653
Kumar, H., Gupta, R., Saraogi, D., et al. 2022, MNRAS, 513, 2777
Laha, S., Barthelmy, S. D., Beardmore, A. P., et al. 2021, GCN, 29939
Landolt, A. U. 1992, AJ, 104, 340
Lazzati, D. 2005, MNRAS, 357, 722
Levan, A. J., Gompertz, B. P., Malesani, D. B., et al. 2023, GCN, 33569
Levan, A. J., Gompertz, B. P., Salafia, O. S., et al. 2024a, Natur, 626, 737
Levan, A. J., Jonker, P. G., Saccardi, A., et al. 2024b, arXiv:2404.16350
Li, L., Liang, E.-W., Tang, Q.-W., et al. 2012, ApJ, 758, 27
Lien, A. Y., Barthelmy, S. D., Beardmore, A. P., et al. 2018, GCN, 23047
Lien, A. Y., Beardmore, A. P., Page, K. L. & Neil Gehrels Swift Observatory Team 2021, GCN, 29930
Lightkurve Collaboration, Cardoso, J. V. d. M., Hedges, C., et al., 2018 Lightkurve: Kepler and TESS time series analysis in Python, Astrophysics Source Code Library, ascl:1812.013
Lipunov, V., Gorbovskoy, E., Kornilov, V., et al. 2020a, GCN, 27555
Lipunov, V., Kornilov, V., Gorbovskoy, E., et al. 2020b, GCN, 28348
Lipunov, V., Yurkov, V., Gabovich, A., et al. 2020c, GCN, 27556
Liu, Y., Sun, H., Xu, D., et al. 2024, arXiv:2404.16425
Mailyan, B., Hamburg, R. & Fermi GBM Team 2020, GCN, 27558
Markwardt, C. B., Barthelmy, S. D., Krimm, H. A., et al. 2023, GCN, 33941
Meegan, C., Lichti, G., Bhat, P. N., et al. 2009, ApJ, 702, 791
Mészáros, P., & Rees, M. J. 1997, ApJ, 476, 232
Mészáros, P., & Rees, M. J. 1999, MNRAS, 306, L39
Mo, G., Jayaraman, R., Fausnaugh, M., et al. 2023, ApJL, 948, L3
Molinari, E., Bondar, S., Karpov, S., et al. 2006, NCimB, 121, 1525
Molinari, E., Vergani, S. D., Malesani, D., et al. 2007, A&A, 469, L13
Moskvitin, A. 2020, GCN, 27570
Moskvitin, A., Pozanenko, A., Moiseev, A., et al. 2023a, GCN, 33871
Moskvitin, A. S., Spiridonova, O. I., Maslennikova, O. A. & GRB follow-up Team 2023b, GCN, 33921
Moss, M. J., Barthelmy, S. D., D'Ai, A., et al. 2023, GCN, 34623
Narayana Bhat, P., Meegan, C. A., von Kienlin, A., et al. 2016, ApJS, 223, 28
Nava, L., Sironi, L., Ghisellini, G., Celotti, A., & Ghirlanda, G. 2013, MNRAS, 433, 2107
Oganesyan, G., Karpov, S., Salafia, O. S., et al. 2023, NatAs, 7, 843
Oganesyan, G., Nava, L., Ghirlanda, G., Melandri, A., & Celotti, A. 2019, A&A, 628, A59
Ogawa, F., Adachi, R., Hosokawa, R., et al. 2020, GCN, 27576
Page, K. L., Beardmore, A. P., Ambrosi, E., et al. 2020, GCN, 27561
Palmer, D. M., Barthelmy, S. D., Cenko, S. B., et al. 2020, GCN, 27311
Palmer, D. M., Barthelmy, S. D., Cummings, J. R., et al. 2021, GCN, 29838
Panaitescu, A., & Kumar, P. 2002, ApJ, 571, 779
Panaitescu, A., & Kumar, P. 2007, MNRAS, 376, 1065
Park, H. S., Ables, E., Band, D. L., et al. 1997a, ApJ, 490, 99
Park, H. S., Williams, G. G., Ables, E., et al. 1997b, ApJL, 490, L21
Parsotan, T., Barthelmy, S. D., Krimm, H. A., et al. 2022, GCN, 32264
Perley, D. A. 2021, GCN, 29549
Perley, D. A., Ho, A. Y. Q., Fausnaugh, M., et al. 2024, arXiv:2401.16470
Piotrowski, L. W. 2012, A&A, 540, L8
Planck Collaboration, Aghanim, N., Akrami, Y., et al. 2020, A&A, 641, A6
Preece, R. D., Briggs, M. S., Mallozzi, R. S., et al. 2000, ApJS, 126, 19
Prentice, S. J., Mazzali, P. A., Pian, E., et al. 2016, MNRAS, 458, 2973
Racusin, J. L., Karpov, S. V., Sokolowski, M., et al. 2008, Natur, 455, 183
Rastinejad, J. C., Gompertz, B. P., Levan, A. J., et al. 2022, Natur, 612, 223
Rhoads, J. E. 1999, ApJ, 525, 737
Richardson, D. 2009, AJ, 137, 347
Ricker, G. R., Atteia, J. L., Crew, G. B., et al. 2003, in AIP Conf. Ser. 662, Gamma-Ray Burst and Afterglow Astronomy 2001: A Workshop Celebrating the First Year of the HETE Mission, ed. G. R. Ricker & R. K. Vanderspek (Melville, NY: AIP), 3
Ricker, G. R., Winn, J. N., Vanderspek, R., et al. 2015, JATIS, 1, 014003
Ridden-Harper, R., Rest, A., Hounsell, R., et al. 2021, arXiv:2111.15006
Roxburgh, H., Ridden-Harper, R., Lane, Z. G., et al. 2023, arXiv:2307.11294
Sagar, R., Kumar, B., & Sharma, S. 2020, JApA, 41, 33
Sakamoto, T., Barthelmy, S. D., Cummings, J. R., et al. 2020, GCN, 28344
Sakamoto, T., Barthelmy, S. D., Krimm, H. A., et al. 2021, GCN, 30554
Sakamoto, T., Barthelmy, S. D., Krimm, H. A., et al. 2022, GCN, 32970
Sakamoto, T., Hullinger, D., Sato, G., et al. 2008, ApJ, 679, 570
Sari, R., & Piran, T. 1999a, ApJ, 520, 641
Sari, R., & Piran, T. 1999b, ApJL, 517, L109
Sari, R., Piran, T., & Halpern, J. P. 1999, ApJL, 519, L17
Sari, R., Piran, T., & Narayan, R. 1998, ApJL, 497, L17
Sbarufatti, B., Page, K. L., Parsotan, T. M., et al. 2022, GCN, 32243
Schlafly, E. F., & Finkbeiner, D. P. 2011, ApJ, 737, 103
Simpson, K. K., Barthelmy, S. D., Gropp, J. D., et al. 2020, GCN, 28335
Smith, K. L., Ridden-Harper, R., Fausnaugh, M., et al. 2021, ApJ, 911, 43
Sonbas, E., Eyles-Ferris, R. A. J., Gronwall, C., et al. 2023, GCN, 33761
Srinivasaragavan, G. P., O'Connor, B., Cenko, S. B., et al. 2023, ApJL, 949, L39
Stamatikos, M., Barthelmy, S. D., Cummings, J. R., et al. 2018a, GCN, 23264
Stamatikos, M., Barthelmy, S. D., Cummings, J. R., et al. 2018b, GCN, 23365

Stecklum, B., Klose, S., Melnikov, S., & Nicuesa Guelbenzu, A. 2020, GCN, 27582

Strausbaugh, R., & Cucchiara, A. 2021, GCN, 29547

STScI Development Team, 2018 synphot: Synthetic photometry using Astropy, Astrophysics Source Code Library, ascl:1811.001

Tarnopolski, M. 2015, A&A, 581, A29

Troja, E., Lipunov, V. M., Mundell, C. G., et al. 2017, Natur, 547, 425

Ukwatta, T. N., Barthelmy, S. D., Cummings, J. R., et al. 2020, GCN, 27443

Ukwatta, T. N., Barthelmy, S. D., Cummings, J. R., et al. 2021, GCN, 29561

van Paradijs, J., Groot, P. J., Galama, T., et al. 1997, Natur, 386, 686

van Roestel, J., Bellm, E. C., Duev, D. A., et al. 2019, RNAAS, 3, 136

Vanderspek, R., Fausnaugh, M. M., Jayaraman, R., et al. 2023, GCN, 33453

Veres, P., Hamburg, R., Meegan, C. & Fermi GBM Team 2020, GCN, 28340

Vestrand, W. T., Borozdin, K. N., Brumby, S. P., et al. 2002, Proc. SPIE, 4845, 126

Vestrand, W. T., Wozniak, P. R., Wren, J. A., et al. 2005, Natur, 435, 178

Vestrand, W. T., Wren, J. A., Panaitescu, A., et al. 2014, Sci, 343, 38

Vestrand, W. T., Wren, J. A., Wozniak, P. R., et al. 2006, Natur, 442, 172

Vianello, G., Lauer, R. J., Younk, P., et al. 2015, arXiv:1507.08343

Virtanen, P., Gommers, R., Oliphant, T. E., et al. 2020, NatMe, 17, 261

von Kienlin, A., Meegan, C. A., Paciesas, W. S., et al. 2014, ApJS, 211, 13

von Kienlin, A., Meegan, C. A., Paciesas, W. S., et al. 2020, ApJ, 893, 46

Wei, J., Cordier, B., Antier, S., et al. 2016, arXiv:1610.06892

Wijers, R. A. M. J., Rees, M. J., & Meszaros, P. 1997, MNRAS, 288, L51

Williams, G. G., Milne, P. A., Park, H. S., et al. 2008, in AIP Conf. Ser. 1000, Gamma-ray Bursts 2007, ed. M. Galassi, D. Palmer, & E. Fenimore (Melville, NY: AIP), 535

Woosley, S. E., & Bloom, J. S. 2006, ARA&A, 44, 507

Xin, L., Han, X., Li, H., et al. 2023, NatAs, 7, 724

Xin, L. P., Wang, X. F., Zheng, J., et al. 2020, GCN, 27571

Xu, D., Izzo, L., Fynbo, J. P. U., et al. 2021a, GCN, 29432

Xu, D., Schady, P., Heintz, K. E., et al. 2021b, GCN, 29944

Yang, Y.-H., Troja, E., O'Connor, B., et al. 2024, Natur, 626, 742

Yi, S.-X., Wu, X.-F., Zou, Y.-C., & Dai, Z.-G. 2020, ApJ, 895, 94

Yost, S. A., Harrison, F. A., Sari, R., & Frail, D. A. 2003, ApJ, 597, 459

Yost, S. A., Swan, H. F., Rykoff, E. S., et al. 2007, ApJ, 657, 925

Yuan, W., Zhang, C., Chen, Y., & Ling, Z. 2022, in Handbook of X-ray and Gamma-ray Astrophysics, ed. C. Bambi & A. Santangelo (Berlin: Springer), 86

Yuan, W., Zhang, C., Ling, Z., et al. 2018, Proc. SPIE, 10699, 1069925

Zhang, B., Fan, Y. Z., Dyks, J., et al. 2006, ApJ, 642, 354

Zhang, B., & Mészáros, P. 2004, IJMPA, 19, 2385

Zhang, B. B., Zhang, B., Castro-Tirado, A. J., et al. 2018, NatAs, 2, 69

Zhu, Z. P., Xu, D., Jiang, S. Q., et al. 2023, GCN, 33771